

Assessment of the **TOPEX** Altimeter Performance
Using Waveform Retracing

Ernesto Rodriguez and Jan M. Martin
Jet Propulsion Laboratory
California institute of Technology
4800 Oak Grove Dr., Pasadena, CA 91109

Abstract

in order to assess the accuracy of the TOPEX altimeter data, we have reprocessed the raw altimeter waveform data using more sophisticated algorithms than those implemented in the altimeter hardware. We discuss systematic contamination of the waveform which we have observed and its effect on very long wavelength errors. We conclude that these systematic errors are responsible for a very long wavelength error whose peak-to-peak magnitude for the Ku-band altimeter is on the order of 1 cm. We also examine the ability of retracked data to reduce the repeat pass variance, and correct for significant waveheight and acceleration dependent errors. We find that the ground post-processing contains SWH dependent biases which depend on the altimeter fine height correction.

1. Introduction

The TOPEX altimeter [Zieger et al., 1991] is the latest in a distinguished line of altimeters used for oceanographic studies. As such, it has inherited many well tested features of previous altimeters, such as the Seasat and Geosat altimeters, but it has also implemented many new features, such as fully digital on-board signal processing. The purpose of this paper is to provide an independent assessment of the performance of the TOPEX altimeter sea surface height measurements by reprocessing the raw altimeter waveform data from scratch using a more optimal algorithm than was possible to implement using the onboard satellite hardware and subsequent post-processing corrections.

in order to provide a statistically meaningful assessment of the altimeter performance, we use in this study reprocessed, or '(retraced', data for cycles 3 to 27 of the TOPEX mission, excluding cycle 20 when the Poseidon altimeter was turned on. The use of retracing for assessing and improving altimeter performance has been previously advocated by Hayne and Hancock [1990] and by Brenner et al. [1993]. The technique we use here is different from theirs, allowing for faster than real time retracing of the entire TOPEX data set. We are continuing to retrack the data in order to make the improved data product available to the oceanographic community after its quality has been fully ascertained. The use of waveform retracing may be of some importance in enhancing the TOPEX data in light

of systematic contamination found in the TOPEX waveform post-launch. What we know of this contamination is described below, and one of the primary goals of this paper is to assess the order of magnitude biases that such distortions may introduce in the data currently available from the TOPEX project.

In order to correct for known biases in the onboard tracker, ground processing corrections have been applied to correct for effects due to altimeter misprinting, significant wave height (SWH), and the tracker “acceleration lag” described below. It is also the purpose of this paper to assess the efficacy of these corrections since they were implemented in the early phase of the mission, when a very limited data set was available. Hayne et al. (this issue) provide a fuller description of the methods used to obtain those corrections.

2. Estimation Procedure and Waveform Features

The mean waveform for any altimeter can be expressed as a convolution of three terms [Brown, 1977]: the surface impulse response, the specular point probability density function, and the instrument point target response (I'IR). A typical theoretical waveform is shown in figure 1, where we have defined three regions: (1) thermal noise, where there is no signal and the waveform is flat, (2) the leading edge, and (3) the trailing edge. It is the detailed shape of the leading edge and trailing edge, and the precise position of the waveform in the data window relative to the altimeter track point location, which allow estimation of the various parameters: the mean height correction, the significant wave height ($H_{1/3}$), the skewness of the specular point PDF [Lipa and Barrick, 1981], the off-nadir angle, the radar cross-section, and the thermal noise level. In the following paragraphs, we offer a brief description of the estimation algorithm we used to estimate these parameters from the TOPEX waveform data. For a fuller description of the method, the reader is referred to Rodríguez and Martin, 1993], where the exact algorithm with its expected theoretical performance are described in detail.

In principle, the most accurate method available for estimation of these parameters is a maximum-likelihood method which makes full use of the statistics of the waveform returns, including any pulse-to-pulse and bin-to-bin correlations [Rodríguez, 1988]. This method may

be expressed as the minimization of

$$-\ln f_{ML} = \frac{1}{2} \sum_{i=1}^N \left(\ln e_i + \frac{v_i^2}{e_i} \right) \quad (1)$$

where

$$v_i = \sum_{j=1}^M [p_j - P_j(\vec{a})], \quad (2)$$

\vec{a} is the vector of parameters, e_i are the eigenvalues of the return waveform correlation matrix, p_j are the measured return values, and $P_j(\vec{a})$ are the values of the theoretical waveform. While accurate for waveforms uncontaminated by systematic distortions, this method is computationally expensive. In [Rodriguez and Martin, 1993], we introduce a computationally efficient alternative at a small expense in performance. If the bin-to-bin correlation of the waveform is neglected, the maximum-likelihood method reduces to a weighted least-squares method which minimizes

$$-\ln f_{WLS} = \sum_{i=1}^N \left(\frac{p_i - P_i(\vec{a})}{\langle p_i \rangle} \right)^2 \quad (3)$$

In fact the correlation between bins are expected to be small for TOPEX on theoretical and experimental grounds [Rodriguez, and Martin, 1993b], so (3) is in fact very close to optimal.

Since the noise on the waveform is multiplicative, the maximum-likelihood method described above puts the most weight on the regions with the least power. This is appropriate when the data conform with the theoretical model. However, should the instrument itself introduce systematic distortions of the waveform which affect strongly the low power regions, the method will bias the estimated parameters. As we discuss below, we have evidence that the TOPEX altimeter does, in fact, introduce such distortions so that the relative noise in different parts of the waveform no longer conforms to the multiplicative noise model. Since, as of the date of writing, the instrument systematic distortions remain to be fully characterized, we have chosen to weight the data uniformly; i.e., set $\langle p_i \rangle = 1$ in (3) for all i . A fuller discussion of the loss of precision incurred by implementing a simple least squares is presented in [Rodriguez and Martin, 1993].

The following is a brief description of the implementation of the fast retracking algorithm described in detail in [Rodriguez and Martin, 1993]. First, the thermal noise is estimated



using only waveform values in the thermal noise region, and this result is subtracted from the input waveform for subsequent processing. Second, the least square function is linearized around an initial set of guesses for the parameters provided by the Geophysical Data Record (GDR) data initially and after a data outage, or by values produced by a simple tracker internal to the algorithm when continuous data are available. Finally, the linearized minimization problem is quickly solved by singular value decomposition,

Even this linearized problem is, in general, very computationally intensive, since the derivatives of the theoretical waveform with respect to the parameters must be calculated by differencing waveforms generated by numerical triple convolutions as no closed form solutions exist for the theoretical waveform for realistic forms of the PTR. However, by approximating the PTR by a set of Gaussians (for which we can analytically calculate both P and $\frac{\partial P_i}{\partial a_i}$), we can develop analytic expressions for the waveform and its derivatives, and so greatly increase the speed of the matrix generation, and the speed of the whole retracking process. In fact, on our HP 735 desktop workstation, we are able to retrack the two-frequency TOPEX waveform data three times faster than real-time.

The accuracy and error variance of this method are very good in Monte Carlo trials with Gaussian noise added [Rodriguez and Martin, 1993], but the results are still subject to systematic errors if the waveform data does not conform to its theoretical model, and this can skew its parameter estimates. This remark is also true for the onboard altimeter tracker and, until the waveform distortions are fully characterized, it is an open question which will offer the more robust estimates. The one advantage that our method has, however, is that we estimate an additional parameter, the skewness, which may act as a “suck-up” parameter, absorbing some of the waveform distortions.

We will now discuss some of the deviations of the, TOPEX waveform from the ideal of Figure 1, and the modifications to the retracing procedure we generated to reduce the influence of those deviations. First, the ground measurements of the TOPEX instrument PTR were not accurate, apparently due to multiple reflections in the test setup. This remark applies also to the PTR obtained using the internal calibration mechanism on the

satellite. In the absence of additional information we have assumed an ideal sinc^2 PTR which matches the measurements in the main lobe and the first two sidelobes. As discussed above, a set of 127 gaussians was used to model this PTR for the fast algorithm, and the observed waveforms seem consistent with this model, as far as we can tell from the residuals to the waveform fit,

Figure 2 shows the average of all waveforms in cycle 5, pass 22, a descending pass, with SWH less than 1.5m. The more rapid decrease in power in the trailing edge of the waveform compared to Figure 1 is caused by a data compression algorithm implemented for the TOPEX waveforms. For high resolution in time, the TOPEX waveforms initially have 1:28 samples separated by $\Delta t = 3.125\text{nsec}$, and to preserve that accuracy those samples are preserved as they are in the region surrounding the leading edge. To reduce the total data volume to 64 samples/waveform, samples 1-16 and 47-64 are averaged two at a time (Δt for those samples is 6.25 nsec) and samples 65-128 are averaged 4 at a time yielding Δt of 12.5nsec. This algorithm thus has the effect of compressing the trailing edge and producing an apparently steeper trailing edge than is actually present. These features are easily implemented in our estimation algorithm.

The solid line in Figure 2 shows data from the northern hemisphere, while the dashed line represents southern hemisphere data. A similar figure for an ascending pass would show exactly the reverse trend. Note that some features in this waveform show latitude dependence and others do not. This behavior can be understood by the following considerations. The TOPEX altimeter uses two different ways of keeping the leading edge in the tracking window: to make large corrections, the timing of the transmit chirp itself is shifted (the "coarse range correction") by a quantized amount; when smaller corrections need to be made, such as the correction to compensate for the continuous change in the height due to the earth's ellipsoidal shape, a "fine height" correction is applied. The fine height correction consists in shifting the waveform data by multiplying with a ramp in the frequency domain after deramping and band pass filtering [Chelton et al., 1989]. This correction is continually being applied on board, and it may be impossible to recover the original data completely

since the only thing that the tracker sees (also the only thing sent down in the telemetry) is an average of many waveforms, all of them with slightly different fine height corrections. In addition to a time shift, the fine height will cause a wrap-around of the trailing edge of the waveform into the thermal noise region. For TOPEX, in order to accommodate the finite bit length of the onboard computer hardware, the way the fine height was implemented digitally depended on the sign of the height rate, the relative velocity between the satellite and the geoid. Thus the fine height implementation was the same for ascending (descending) passes in the southern hemisphere as for descending (ascending) passes in the northern (southern) hemisphere since they both had the same positive (negative) height rate. The waveform features that move from northern to southern hemisphere do so because their position in the data window is dependent on the fine-height time offset. The patterns shown here are systematic, repeatable, and shift between ascending and descending passes. The stationary features are features of the digital filter response, which is not affected by fine height.

This figure illustrates three systematic waveform errors which required algorithm modification. First, the oscillations just past the leading edge (samples 23--41) are caused by quantization error in the digital filter bank (Jensen and Purdy, private communication, 1993) and are independent of the fine-height adjustment. These fluctuations are also present in the calibration waveform, and since they are stationary, may be removed through normalization by the noise-only calibration measurements. Second, the analog filter passband response causes a rapid decrease in amplitude at the end of the trailing edge, but due to the variation in the fine-height offset and the signal wraparound due to data sampling, a portion of that high-frequency energy is aliased into the first few bins. Since the passband moves with fine-height, the response in the last 3 bins and the first 3 bins (due to wrap-around) varies considerably. This variation is not included in the waveform model and we omitted these bins from the fitting process.

We also note spurious fine height-dependent signals in the waveform, both in the trailing edge and in the thermal noise region of the waveforms. The large magnitude peak in the trailing edge centered on bins 43 and 44 is due partly to a DC bias present in the quantizer,

and partly to an additional spurious signal of unknown origin which moves with fine-height and produces the breadth of 5 bins observed in the average waveforms. This error would produce significant errors in the attitude estimates if not compensated: our solution is again to mask off the affected bins and not include them in the fit.

The closeup of the thermal noise region and the first part of the leading edge shown in Figure 2b shows yet another spurious signal which moves with fine height and significantly affects the form of the initial part of the leading edge, and thus may modify any parameters sensitive to this region. Since this signal extends over a significant part of the thermal noise region and into the leading edge, we could not simply mask off the affected bins. The main effect of the contamination of the thermal noise region will be to cause the estimation algorithm to overestimate the amount of thermal noise and subtract an amount which will artificially lower the power in the leading edge relative to the true value. To partially remove the affect of this localized additional power, we compensated by subtracting only 70% of the estimated thermal noise level. This percent was selected by minimizing the residuals in the region away from the anomaly (bins 3- 12).

In addition to what we can see in Figure 2, there are apparently a pair of peaks related to the signals near DC and also move with the fine-height adjustment (Purdy, private communication, 1992). These features were observed on an actual test of the altimeter hardware and its mock-up. A possible cause for their existence is leakage into the altimeter of another satellite signal and its harmonics, which may show up as the peaks observed in the residuals in the thermal noise region and early parts of the leading edge, but this is only conjecture. Careful measurements suggest that the spikes are present at times within the leading edge of the Ku-band waveform, and for large fractions of the time in the leading edge of the C-band waveform. The estimation results presented below are consistent with that assertion, showing different behavior for the first and last half of each pass, and consistently opposite behavior between ascending and descending passes.

The C-band waveforms are subject to similar errors and corrections, but the presence of the spurious signals in this case is more serious. The waveform in the C-band data window

is moved to the right two bins, which puts the spurious signals right in the leading edge a substantial part of the time.

3. Dynamic Tracker Response and the Acceleration Correction

Every tracker period, the altimeter estimates its range above the ocean surface using the onboard height error estimation algorithm. Due to thermal and speckle waveform noise, this height estimate is noisy and rather than report it directly, the instrument reports the location of the “track point”, the point where its tracking loop expects the true range to be. The track point is derived by passing the raw range estimates through a causal smoothing filter, the “ α -/3 tracker”. This procedure implies that, even for noiseless range estimates, the output spectrum of the altimeter signal will be distorted from the input spectrum.

As far as we know, this distortion has not been fully characterized for altimeter dynamic tracking over a real geoid. In appendix A, we show that for times much greater than the tracker update period ($\tau = 0.05$ sec), which is the typical scale of interest for oceanography, the output signal Fourier coefficients, $c(\omega)$, are related to the input signal spectrum, $b(\omega)$, by the relation

$$c(\omega) = \frac{1}{1 - \frac{\omega^2}{\beta/\tau^2 + i\alpha\omega/\tau}} b(\omega) \equiv T(\omega)b(\omega) \quad (1)$$

This implies that the output signal spectrum will be multiplied by a spectral distortion factor of $|T(\omega)|^2$. In addition, since $T(\omega)$ is complex, the phase of $c(\omega)$ will be shifted relative to that of $b(\omega)$. In Figure 3, the solid line represents a plot of the spectral distortion factor and the relative phase for the frequencies of interest for TOPEX1/sec data. For low frequencies, i.e., when $\omega \ll \beta/\alpha\tau \approx 2\pi/5$ sec and $\omega \ll \sqrt{\beta}/\tau \approx 2\pi/2.5$ sec, the transfer function can be approximated as

$$T(\omega) \approx 1 + \frac{(\omega\tau)^2}{\beta} \quad (2)$$

or equivalently, the output signal, r , is related to the input signal, r' by

$$r(t) \approx r'(t) - \frac{\tau^2}{\beta} \frac{d^2 r'}{dt^2} \quad (3)$$

The estimated range lags behind the true range by a term proportional to the range acceleration. This effect is called the tracker acceleration lag and the TOPEX GDR processing

makes an acceleration correction to try to remove this error. The GDR correction is obtained by estimating the tracker range acceleration using a moving three second data window to estimate the acceleration at a 1/sec rate. This correction has the effect of further distorting the output spectrum. Given a perfect estimate of the true acceleration, the transfer function for the acceleration corrected output signal is given by

$$T''(\omega) = (1 - \frac{(\omega\tau)^2}{\beta})T'(\omega) \quad (4)$$

In Figure 3, the dashed line represents a plot of the modulus squared and phase of $27'(\omega)$. As can be seen from this figure, applying the acceleration correction has the effect of severely attenuating the spectrum in the 0.1 Hz-1 Hz (6 km - 60 km) frequency (spatial) range. This attenuation will distort the spectrum of both the true input signal and any contaminating noise as well. The retracked height estimates are not passed through a tracking filter and will, therefore, not distort the input spectrum aside from introducing uncorrelated estimation noise. Therefore, the tracker spectral distortions may be observed by taking the ratio of the altimeter height output spectrum to the retracked height spectrum.

The TOPEX GDR does not directly report the acceleration correction. Rather, it reports a net instrument correction which consists of low frequency offsets and the higher frequency acceleration correction. To duplicate the acceleration correction, we repeated the fitting procedure outlined in the TOPEX GDR Handbook and verified the procedure by checking that it coincided with the high frequency excursions of the GDR net height correction to better than 2mm. We are thus able to recover the tracker height estimates, prior to the application of the acceleration correction. Figure 4 show the ratios of the TOPEX tracker height spectra, prior and after the application of the acceleration correction, to the retracked height spectra. This figure closely resembles Figure 3, and the departures can be attributed to the presence of estimation noise for the tracker, retracing, and the acceleration corrections.

Since the acceleration correction attenuates the spectrum in the 0.1 Hz-1 Hz frequency range, we have removed the GDR acceleration correction and replaced it with a smoothed acceleration correction obtained by convolving the acceleration correction with a Hanning

(cosine) window whose half-power width is 5 sec. This has the effect of improving the spectral distortion for frequencies smaller than 0.2 Hz., while avoiding excessive spectral attenuation for higher frequencies. An examination of the acceleration correction spectrum shows that neglecting the high frequency part of the acceleration correction introduces very small errors for most cases encountered in practice. We will use this corrected height in all the comparisons presented below.

4. The Estimated Skewness

The sea surface skewness is the estimated parameter most sensitive to noise. As such, we expect any systematic waveform distortion effects due to the fine height dependent contamination to show most clearly in this parameter. Figure 5 shows Ku-band estimated skewness, averaged over all cycles and longitudes, and segregated by whether the pass is ascending or descending. A sudden transition at the equator is apparent, the sense of the transition depending on the sense of the transition of the fine height rate at the equator. This is exactly the type of transition found in the waveform fitting residuals and in the bench test of the TOPEX hardware (C. Purdy, personal communication). What we suspect is happening is the following: hardware tests have shown that for Ku-band, a power spike migrates in and out of the leading edge region depending on which sign the relative velocity between the satellite and the earth's surface has. The effect of the true surface skewness is to remove power from the center of the leading edge and redistribute it to the edges of the leading edge. The effect of a contaminating power spike will be to **lower** the value of the estimated skewness if it happens to be in the center of the leading edge, and to **raise** it if it *happens* to be in one of the sides of the leading edge. We speculate that the very low values, including some negative ones, for the estimated skewness observed in the southern hemisphere in ascending passes and the northern hemisphere on descending passes are due to this waveform distortion. To estimate the magnitude of the jump, we fit a function of the form

$$f = a_0 + a_1 \text{sign}(\theta) + a_2 \sin(2\theta) - a_3 \cos(2\theta) \quad (5)$$

where θ is the latitude. The results are also shown in Figure 5, which show that the main effect of the waveform distortion, assuming that the averaged skewness has a global mean value, is to introduce a jump of $\sim \pm 0.02$ at the equator. This is not a very large jump, but it does introduce uncertainties about the true mean value of the sea surface skewness.

To test whether the estimated skewness behavior is physically reasonable, aside from the discontinuity at the equator, we examined its behavior against the parameter ρ defined by

$$\rho = \frac{U}{\sqrt{gH_{1/3}}} \quad (6)$$

where U is the wind speed estimated from the GDR σ_0 using the model function of Witter and Chelton [1991], and $H_{1/3}$ is the significant wave height. This parameter, proportional to the square root of the ratio between the wind kinetic and wave potential energies, has been shown to be empirically related to the wave age for maturing seas [Hasselmann et al., 1976], and for surprisingly large values of the wave age [Glazman and Pilorsz, 1990]. Following Hasselmann et al. [1976] and Kahma [1981], we will assume that the lowest wavenumber of a wind driven sea spectrum can be written as

$$k_0 = (20)^2 \frac{g}{U^2} x^{-2/3} \quad (7)$$

where x is the dimensionless fetch. We further assume that the following well known relationship [Hasselmann et al., 1976], [Kahma, 1981], [Glazman et al., 1988] between the dimensionless fetch and $H_{1/3}$ and U holds:

$$x \approx 3.9 \times 10^5 \rho^{-4} \quad (8)$$

This allows us to estimate k_0 as a function of the altimeter observable alone. Given this parameter, the significant slope [Huang and Long, 1980] for the spectrum can be expressed as

$$s = \frac{k}{k_0} \quad (9)$$

Srokosz and Longuet-Higgins [1986] have derived limits for the value of λ as a function of significant slope. For a surface wave spectrum, $F(k) \sim k^{-p}$, characterized by a spectral

decay constant p , the sea surface skewness was shown to be bounded by the relation

$$0 \leq 4 \left(4 - 12\pi s \frac{p-1}{2p-3} \right) \leq \lambda \leq 1.01 \left(12\pi s \frac{p-1}{2p-3} \right) \quad (10)$$

Figure 6 shows the behavior of the data and the theoretical bounds for two values of p : $p = 4$ (the Phillips [1980] spectrum) and $p = 3.5$ a spectral form proposed by Kitaigorodskii [1983] and Phillips [1985]. This figure shows that, aside from an over all constant bias, the estimated skewness follows the theoretical trend quite closely. This encourages us to believe that, although contaminated by leakage, it still offers a measurement reflecting ocean physics.

Figure 7 presents the longitude-averaged skewness results for the C-band altimeter. We notice that the equatorial transition is greatly enhanced, giving rise to larger discontinuities and an overall shift of the mean skewness value toward greater skewness. The C-band altimeter leading edge is placed at a different location relative to zero frequency than the Ku-band waveform. The location has, in fact, been shown to be contaminated by power leakage to a greater extent than its Ku-band counterpart (C. Purdy, personal communication). We suspect this is the cause for the greater contamination of the skewness estimate. This will be corroborated below, where we study the effects of the height rate on the height measurements.

5. Assessment of TOPEX Height Estimation Performance

The retracked height correction can be thought of as consisting of five parts: 1) a correction to the tracker dynamic response, including the acceleration lag; 2) a correction to the onboard tracker $H_{1/3}$ and attitude dependent biases; 3) a correction to the bias induced on the onboard tracker by the (surface or effective) skewness; 4) a correction to the onboard tracker jitter; 5) estimation noise. To compare against the GDR heights, we look at the residual between the retracing correction and the two corresponding corrections in the GDR: the acceleration and the SWH-attitude correction,

Very Long Wavelength Behavior

The residual and skewness results lead us to examine the behavior of the residual between the retracked and GDR corrections as a function of latitude, segregated by ascending or descending pass direction. Figure 8a shows the behavior of the difference between the retracking correction and the GDR SW II-attitude correction, not including the GDR acceleration. For long wavelengths, the acceleration correction is dominated by the ellipsoidal shape of the geoid. For a circular geoid, the sea surface height correction due to the tracker lag can be shown to be

$$\delta h = - \frac{\tau^2}{\beta} (R_e - R_p) \Omega^2 \cos(2\theta) \quad (11)$$

$$\approx -0.7 \cos(2\theta) \quad (12)$$

where R_e and R_p are the equatorial and polar radii, respectively, and Ω is the angular frequency of the satellite. We have fit the residual shown in Figure 8 with a function of the form given by equation (5) and the results, (presented in the figure) show that the cosine term is indeed of the right magnitude and sign for both ascending and descending passes. A small discontinuity ($\sim 2\text{mm}$) can be seen at the equator, but the main additional effect is due to a $\sin(2\lambda)$ term which switches sign depending on whether the pass is ascending or descending; i.e. depending on the sign of the height rate. These results are emphasized in Figure 8b which presents the residual correction after using the GDR SWH-attitude correction and the GDR acceleration correction. The cosine term due to the geoid has been removed, but the $\sin(2\theta)$ term remains as a residual error whose peak to peak magnitude is approximately 1 cm.

To investigate the source of this term, we studied the behavior of the residual correction as a function of $H_{1/3}$, again segregating the data into ascending and descending passes. The result is shown in Figure 9. There is a clear separation of the results by both SWH and the sign of the height rate. The discontinuities shown are due to the fact that the on board tracker behaves differently for each tracking mode (or tracking index) chosen. We speculate that these systematic differences are due to changes in the degree of waveform contamination as the leading edge broadens to include more fine height dependent distortions. Notice that,

by happenstance, the systematic errors are such that if all the data are averaged only a very small $H_{1/3}$ dependent bias will be observed.

Theoretically [Srokosz, 1986], [Rodriguez , 1988] skewness (ocean or waveform) should bias the onboard tracker by an amount whose upper bound is given by $\lambda H_{1/3}/24$ if no provisions have been made to account for the skewness bias, For TOPEX, the height corrections were calculated on the assumption of a constant waveform skewness of 0.1 (G. Hayne, personal communication). This will have the effect of shifting the origin of the skewness bias vs. $\lambda H_{1/3}/24$, but leaving the linear trend the same. Figure 10 presents a plot of the residual height error against $\lambda H_{1/3}$. The linear trend is clear, although the slope is a little smaller than the upper bound and is greatly reduced when the SWH is large, as can be seen by the sudden transition which corresponds to a transition in gate index to higher SWH. These features were discussed at great length in [Rodríguez , 1988] and the reader should refer to that paper for further details.

Figure 11 presents the average latitude behavior of the C-band height residual errors. The discontinuity at the equator is the clear dominating feature. Its greater magnitude was expected from the degree of contamination exhibited by the C-band skewness. The C-band residual height error has a peak to peak signature of approximately 2 cm. Since this height is only used to estimate the ionospheric correction, these errors will be diminished by a factor of 6.4, the ratio of the Ku- and C-band frequencies squared. Therefore the signature will not be apparent as a jump at the equator,

Short and Medium Wavelength Behavior

To study the intermediate wavelength (10 km -6000 km) signature of the residual errors, characterize the improvements offered by retracking, and to offer an independent verification of its efficacy, we studied the spectral characteristics of the residual error and the sea surface height and sea surface height variability spectra. Figure 12 presents the spectra of the retracking height correction, and the GDR acceleration and SWH-attitude corrections, as well as the spectrum of the residual correction, The retracing correction has more power at higher frequencies for two reasons: 1) it contains estimation noise; and 2) it must correct for

the tracker jitter noise. In fact, we have seen that the retracking correction is anticorrelated with the GDR sea surface height measurement for frequencies greater than 0.1 Hz, after which the ocean signal is much larger than the tracker jitter. This anticorrelation is what we would expect if the retracing correction is in fact a correction, rather than just additional noise. The residual correction is greatest at the longest frequencies, and this difference is probably due, to both the SWH and skewness trends discussed above,

If the retracking correction reduces noise and improves on the low-frequency acceleration correction, one should observe a drop in the spectrum of sea surface height, where we expect little or no oceanographic signature. To confirm this, we calculate the spectrum of height, obtained by subtracting the Rapp mean sea surface [GDR Users Handbook] from the altimeter measurements using track segments for which 1024 seconds of contiguous data were present in the GDR. The results are shown in Figure 13, where the ratios of the corrected height with the “raw” (no acceleration or SWH-attitude corrections) height are displayed. As we Intentioned above, the SWH-attitude and the smoothed acceleration correction we applied improves on the raw height for frequencies lower than 0.2 Hz. The improvements made by the raw retracking correction, and a version of the retracing correction which has been smoothed with the same Hanning window as the acceleration correction, are greater. The reduction in variance made by the retracking correction over the GDR heights is presented in Figure 15a, where we plot the quantity

$$\Delta r = \left[\int_{\text{upper}} dk F_{\text{GDR}}(k) \cdot F_{\text{Retrack}}(k) \right]^{1/2} \quad (13)$$

where $F(k)$ represents the sea surface spectrum. This figure shows that the raw retracked height decreases the variance by $\sim (1.2\text{cm})^2$, while the smoothed retracked correction reduces the variance by $\sim (0.8\text{cm})^2$. Most of the gains are made at the higher frequencies, although there is a further improvement at lower frequencies, as should be expected from the long wavelength results.

As a further verification of the retracing improvements, we calculated the sea surface height variability spectrum by taking the difference of the sea surface heights with a mean sea surface calculated by averaging the data over all the cycles used and using the technique

introduced by Chelton et al. [1990]. The results are shown in Figure 14. The raw retracked height shows an improvement at high and low frequencies, but a slight deterioration for frequencies around 0.1 Hz. This can be understood as follows: for variability studies, the acceleration correction drops out since the error is geographical. The remaining contributions from the retracing correction are due to the tracker jitter, which it improves at the highest frequencies, the SWH-attitude correction, which is very small at frequencies of 0.1 Hz, and estimation noise, which becomes important at these frequencies. These considerations motivate us to apply the smoothed retracking correction for variability studies since the filtering will suppress the estimation noise. Figure 14 shows that this is in fact the case and that applying the smoothed acceleration correction (which is not equivalent to smoothing the sea surface itself) reduces the repeat pass variance. The extent to which this is true is shown in Figure 15b which is the variability counterpart of Figure 15a. Notice that for the purpose of variability studies, the GDR SWH-attitude and acceleration corrections make 1110 reduction in the repeat pass variance.

6. Conclusions

We have examined the accuracy of the TOPEX GDR height data using retracing of the altimeter raw waveform data, which allows for a more optimal extraction of the sea surface information contained in it. In agreement with hardware tests, we found that the on board waveform had been contaminated with leakage whose characteristics depended on the sign of the height rate. For the main altimeter channel, Ku-band, the retracing differed from the GDR heights by a long wavelength signal whose peak to peak signature is on the order of 1 cm. For shorter wavelengths, we showed the variance reduction capabilities of the retracked data at the 1 cm level. We also pointed out potential problems at high frequencies due to the way the acceleration correction is applied in the GDR and suggested an alternative approach. Finally, we showed that the estimated sea surface skewness, while contaminated by the waveform artifacts, showed qualitative agreement with theoretical predictions. We are presently investigating ways of removing the fine height dependent corrections from the waveform data in order to provide high quality sea surface height,

Appendix A

The $\alpha - \beta$ tracker implemented in TOPEX is quite complex when described on time scales of the tracker update time ($\tau = 0.005$ sec). However, for longer times, the tracker can be adequately modeled by the coupled pair of difference equations for the range, r_n and range rate v_n

$$r_{n+1} = r_n + v_n \tau + \alpha(\rho(t) - r_n) \quad (14)$$

$$v_{n+1} = v_n + \frac{\tau}{\tau^2} \beta(\rho(t) - r_n) \quad (15)$$

where $\rho(t)$ is the input range, $\alpha = 1/4$, and $\beta = 1/64$. For $\rho(t)$ consisting of frequencies much smaller than $1/\tau$, we can replace these equations by the coupled set of differential equations

$$\frac{dr}{dt} = \frac{\alpha}{\tau}(\rho(t) - r) + v \quad (16)$$

$$\frac{dv}{dt} = \frac{\beta}{\tau^2}(\rho(t) - r) \quad (17)$$

This is equivalent to the following second order differential equation for the tracker range

$$\frac{d^2 r}{dt^2} + \frac{\alpha}{\tau} \frac{dr}{dt} + \frac{\beta}{\tau^2} r = \frac{\alpha}{\tau} \frac{d\rho}{dt} + \frac{\beta}{\tau^2} \rho \quad (18)$$

The homogeneous solution to this equation is a decaying exponential with a time constant of 0.4sec, which is shorter than the typical periods we will be concerned with and we will neglect this term henceforth.

We solve this equation by taking the Fourier transform of both sides and solving for $c(\omega)$, the Fourier coefficient of the tracker range, in term of $b(\omega)$, the Fourier coefficient of the input range, to get

$$c(\omega) = \frac{1}{1 - \frac{\omega^2}{\beta/\tau^2 + i\alpha\omega/\tau}} b(\omega) \equiv T(\omega) b(\omega) \quad (19)$$

In the derivation above, we have used the Fourier transform convention

$$r(t) = \frac{1}{2\pi} \int d\omega c(\omega) e^{i\omega t} \quad (20)$$

Acknowledgement

The research described in this paper was carried out by the Jet Propulsion Laboratory, California Institute of Technology, under contract with the National Aeronautics and Space Administration. We would like to thank P. Callahan, L. Fu, D. Imel, C. Morris of JPL, D. Hancock, G. Hayne, C. Purdy of NASA Wallops/Goddard and R. Jensen of APL-JHU for sharing their early results with us and giving us helpful comments. We would also like to thank K. Wiedman for her useful comments.

References

- Brenner, A. C., C.J. Koblinsky, and H.J. Zwally, "Postprocessing of satellite altimetry return signals for improved sea-surface topography accuracy," *J. Geophys. Res.*, 98, C1, 933-944, 1993.
- Brown, G. S., "The average impulse response of a rough surface and its applications," *IEEE Trans. Antennas Propag.*, AP-25(1), 67-74, 1977.
- Chelton, D., Walsh, E. J., MacArthur, J. L., "Pulse compression and sea level tracking in satellite altimetry," *J. Atmos. and Oceanic Tech.*, Vol. 6, no. 3, 407-437, 1989.
- Chelton, D.B., Schlax, M. G., Witter, D. L., Richman, J. G., "Geosat altimeter observations of the surface circulation of the southern ocean," *J. Geophys. Res.*, 95, NC10, 17887-17903, 1990.
- Glazman, R. E., Pilorz, S. H., "Effects of sea maturity on satellite altimeter measurements," *J. Geophys. Res.*, 95, NC3, 2857-2870, 1990.
- Hayne, G. S., and D. W. Hancock, "Corrections for the effects of significant wave height and attitude on Geosat radar altimeter measurements," *J. Geophys. Res.*, 95, C3, 2837-2842, 1990.
- Hasselmann, K., Ross, L., Muller, P., Sell, W., "A parametric wave prediction model," *J. Phys. Ocean.*, 6, 200-228, 1976.

- Huang, N.F., Long, S.R., "An experimental study of the surface elevation probability distribution and statistics of wind-generated waves," *J. Fluid Mech.*, 101, 179-200, 1980.
- Kahma, K. K., "A study of the growth of the wave spectrum with fetch," *J. Phys. Oceanogr.*, 11, 1503-1515, 1981.
- Kitaigorodskii, S. A., "On the theory of the equilibrium range in the spectrum of wind generated gravity waves," *J. Phys. Ocean.*, 13, 816-827, 1983,
- Lipa, B.J., and D.E. Barrick, "Ocean surface height-slope probability density function from Seasat altimeter echo," *J. Geophys. Res.*, 86 (C11), 10,921-10,930, 1981.
- Phillips, O. M., *The Dynamics of the Upper Ocean*, Cambridge university Press, New York, 1980.
- Phillips, O. M., "Spectral and statistical properties of the equilibrium range in wind-generated gravity waves," *J. Fluid Mech.*, 156, 505-531, 1985.
- Rodriguez, E., "Altimetry for non-Gaussian oceans: height biases and estimation of parameters," *J. Geophys. Res.*, 93, C11, 14,107-14,120, 1988.
- Rodríguez, E., and Martin, J. M., "Correlation properties of altimeter returns," *IEEE Geosci.*, in press.
- Rodríguez, E., and Martin, J. M., "A fast algorithm for altimeter waveform retracing with applications to the Geosat Altimeter," submitted to *J. Ocean. Tech.*, 1993.
- Srokosz, M. A., and M. Longuet-Higgins, "On the skewness of sea surface elevation," *J. Fluid Mech.*, 164, 487-497, 1986.
- Witter, D.L., and Chelton, D.B., "A Geosat altimeter wind-speed algorithm and a method for altimeter wind-speed algorithm development," *J. Geophys. Res.*, 96, NC5, 8853-8860, 1991.

Zieger, A.R., D.W. Hancock, G.S. Hayne, and C.L. Purdy, "NASA radar altimeter for the Topex Poseidon project," Proc. IEEE, 79(6), 810-826, 1991.

Figure Captions

Figure 1. A typical altimeter waveform generated using the triple convolution theory and TOPEXPTR approximated by 127 gaussians. Other parameters also consistent with TOPEX values.

Figure 2. (a) Average of TOPEX waveforms for cycle 5, pass 22, $H_{1/3} < 1.5\text{m}$ for northern (solid) and southern (dashed) latitudes. Note deviations from ideal waveform of Figure 1. The more rapid decrease of power in the latter part of the trailing edge is due to TOPEX compression of 2 and 4 bins averaged together in that part of the waveform. The very steep rolloff at the very end of the trailing edge is the analog filter response. (b) Closeup of the thermal noise region and beginning of the leading edge.

Figure 3. The amplitude squared (a) and phase (b) response of the α - β tracker for TOPEX. The solid curve is the tracker alone, and the dashed curve includes the acceleration correction. Note the significant variation in the 0.2- 0.5 Hz range.

Figure 4. The ratio of the spectrum of the GDR height correction with (+) and without (A) the acceleration correction to the spectrum of the retracked height correction. Note the significant suppression by the acceleration correction of all high-frequency height variation.

Figure 5. Mean (solid) of skewness estimates for ascending and descending data passes averaged over 0.5° of latitude and all longitudes plotted vs. latitude. The (+) signs represent the variance of the skewness value after averaging over $0.5^\circ \times 0.5^\circ$ latitude-longitude boxes. The dashed lines plot the results of fitting a sinusoidal, 2 cycles per orbit function with an offset at the equator. The results clearly show a dependence on range-rate sign, which makes estimating surface, rather than effective, skewness problematical.

Figure 6. Ku-band skewness estimates separated by north/south and ascending/descending, and binned by ρ . Theoretical bounds on expected skewness for a power-law ocean with $p = 4$ (long dash) and $p = 3.5$ (short. dash) also shown. Note the relative consistency of the pre- and post-equator parts of each pass. Though the absolute values of the skewness are just barely consistent with theory, the form of the ρ dependence is consistent.

Figure 7. Mean (solid) and standard deviation (+) of latitudinal average of C-band

skewness estimates for ascending and descending passes. Dashed lines show fits as in Figure 5.

Figure 8. Means (solid) and standard deviations (+) of difference of retracked height correction and GDR SWH-attitude height correction for ascending (a) and descending (b) passes, Data dominated by large-scale geoid contribution to the acceleration error. Acceleration correction is included in (c) and (d), which reduces error to 1 cm peak-to-peak.

Figure 9. Same data as Figure 8 (c) and (d) again separated by latitude and path direction, and binned by SWH. Note differences between as before between pre- and post-equator parts of the pass, and differing dependence on SWH.

Figure 10. Comparison of height residuals with theoretical skewness bias of $\lambda H_{1/3}$. The change in the slope of the curves is due to a change in the tracking gate size, as discussed in [Rodriguez , 1988].

Figure 11. C-band height correction residuals and standard deviations including acceleration correction. Errors show peak-to-peak variation of 2cm and jump of 1 cm at the equator. Anomalous value at 22 deg is due to a single point and may be ignored.

Figure 12. (a) Spectra of GDR SWH-attitude, acceleration, and retracked height corrections vs. inverse spatial frequency. (b) Spectrum of difference of total GDR correction and retracked correction.

Figure 13. (a) Spectral density of the sea-surface height calculated from retracked data. (b) Ratio of spectrum of GDR height with no corrections to the height spectra for heights corrected by the full (raw) retracked height correction (\diamond), spectra of heights corrected by a Hanning-smoothed retracked height correction (A), and GDR heights using a smoothed acceleration correction (+). Note the greatest reduction in variance is produced by the full retracked result.

Figure 14. (a) Spectra of difference between retracked (solid) of GDR (dashed) sea surface height estimates and the mean height values at that position (variability spectrum). (b) Ratios of raw (uncorrected) altimeter height spectrum to raw retracked (\diamond), smoothed retracked (\triangle), and GDR (+) height variability spectra. The greatest reduction in variability

variance is achieved with the smoothed retracked data.

Figure 15. (a) integral of height variance reduction spectrum for raw retracked data (dashed) and smoothed retracked data (solid). (b) Same as (a), but variability spectra instead of absolute height spectra. Note consistency with results of Figures 13 and 14.

Mean Altimeter Waveform

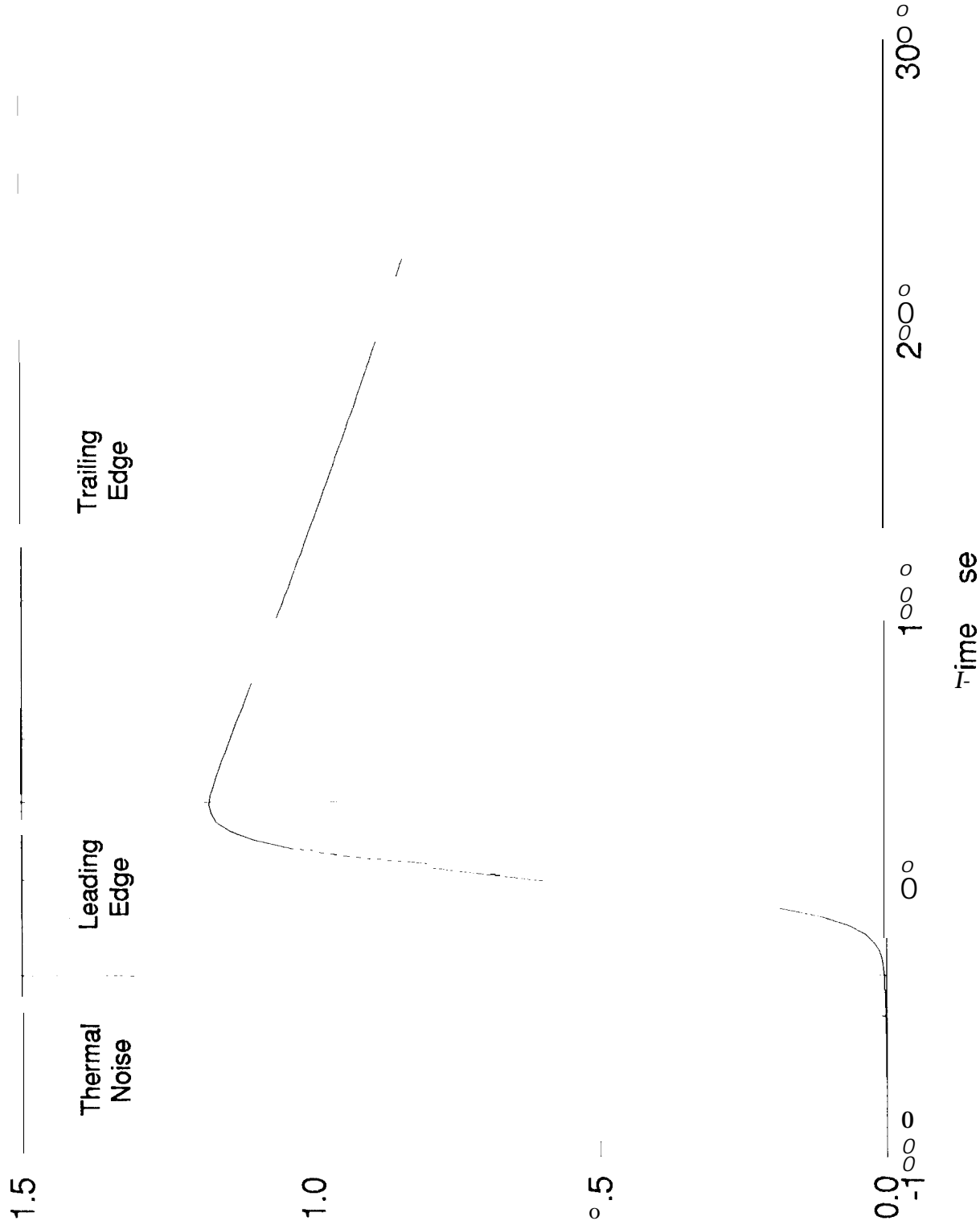
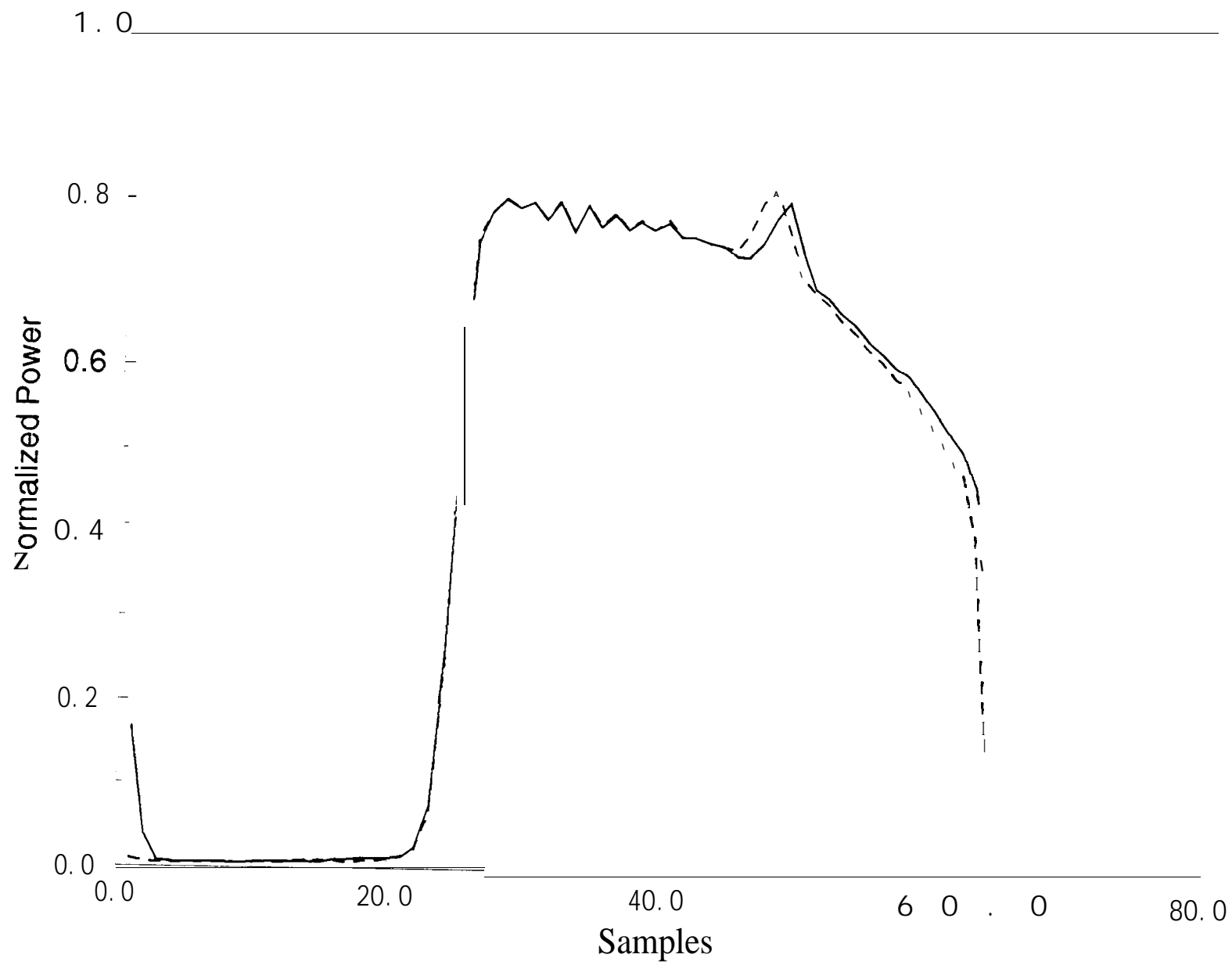
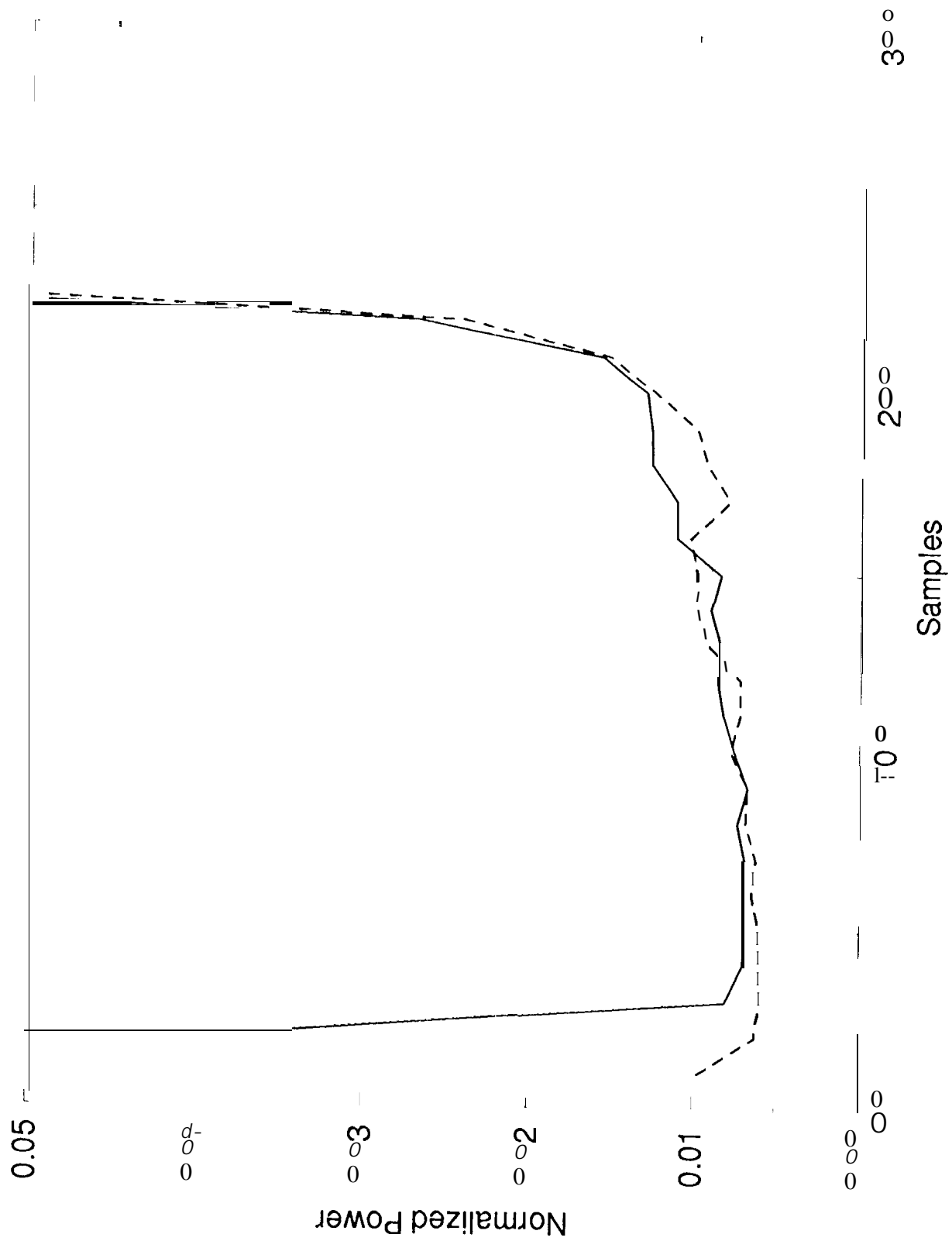


Figure 1





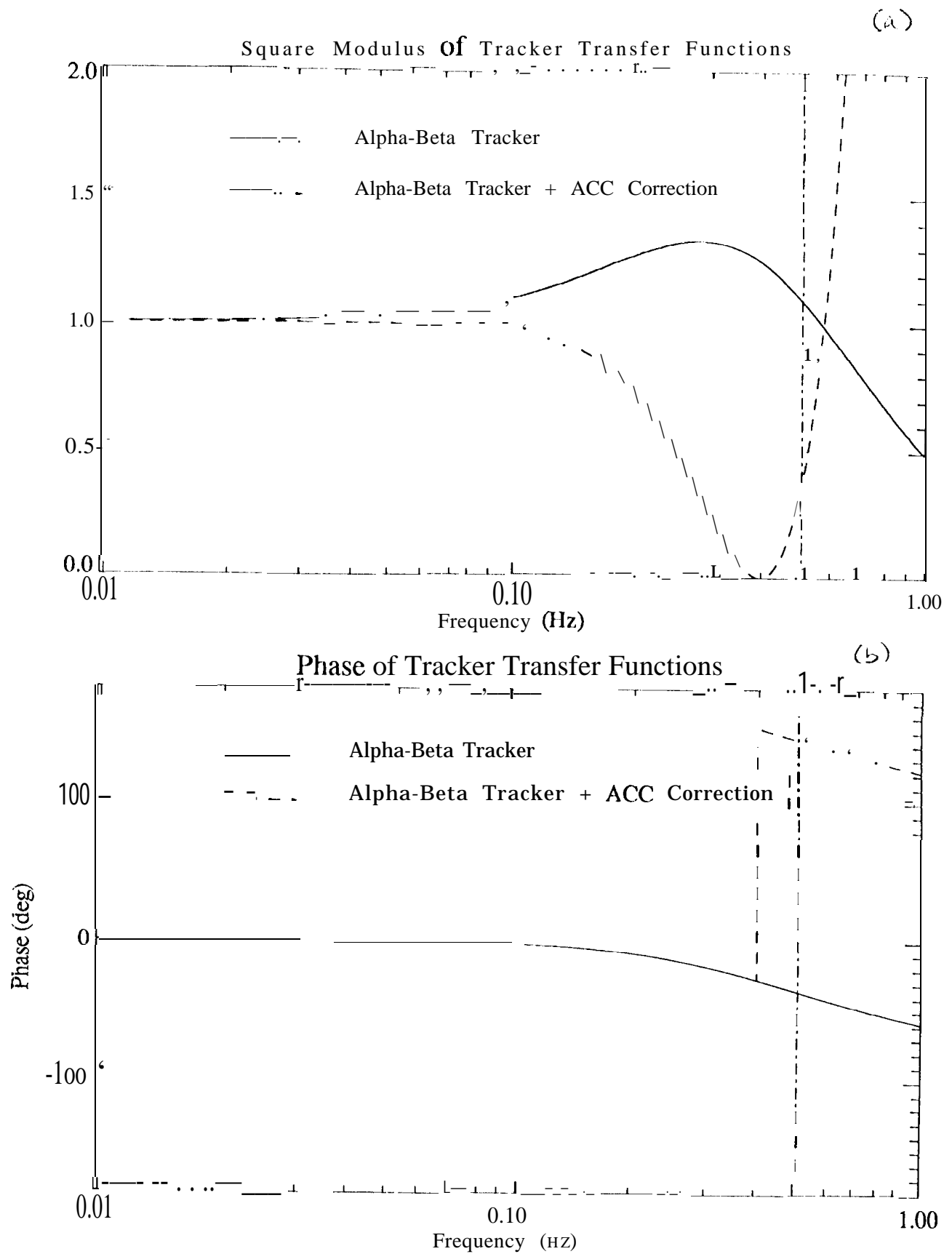


Figure 3

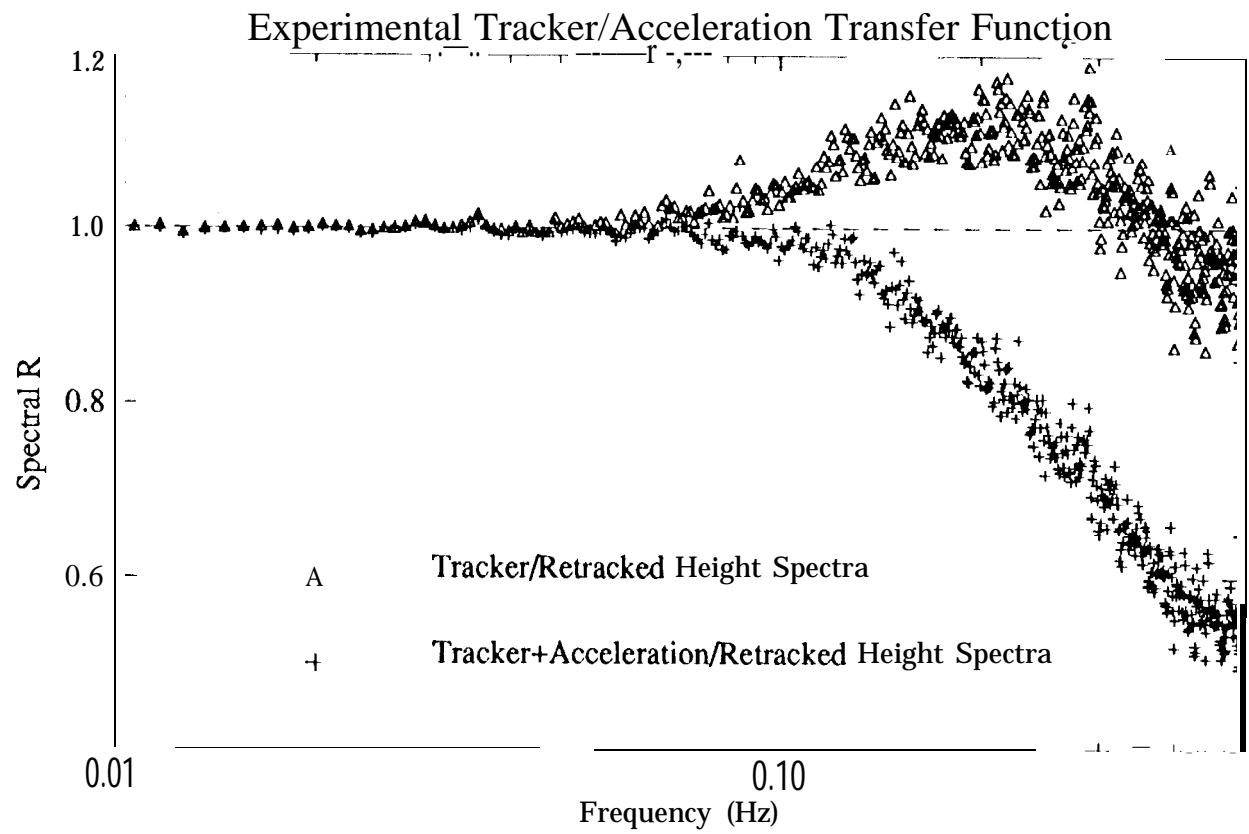


Figure 4

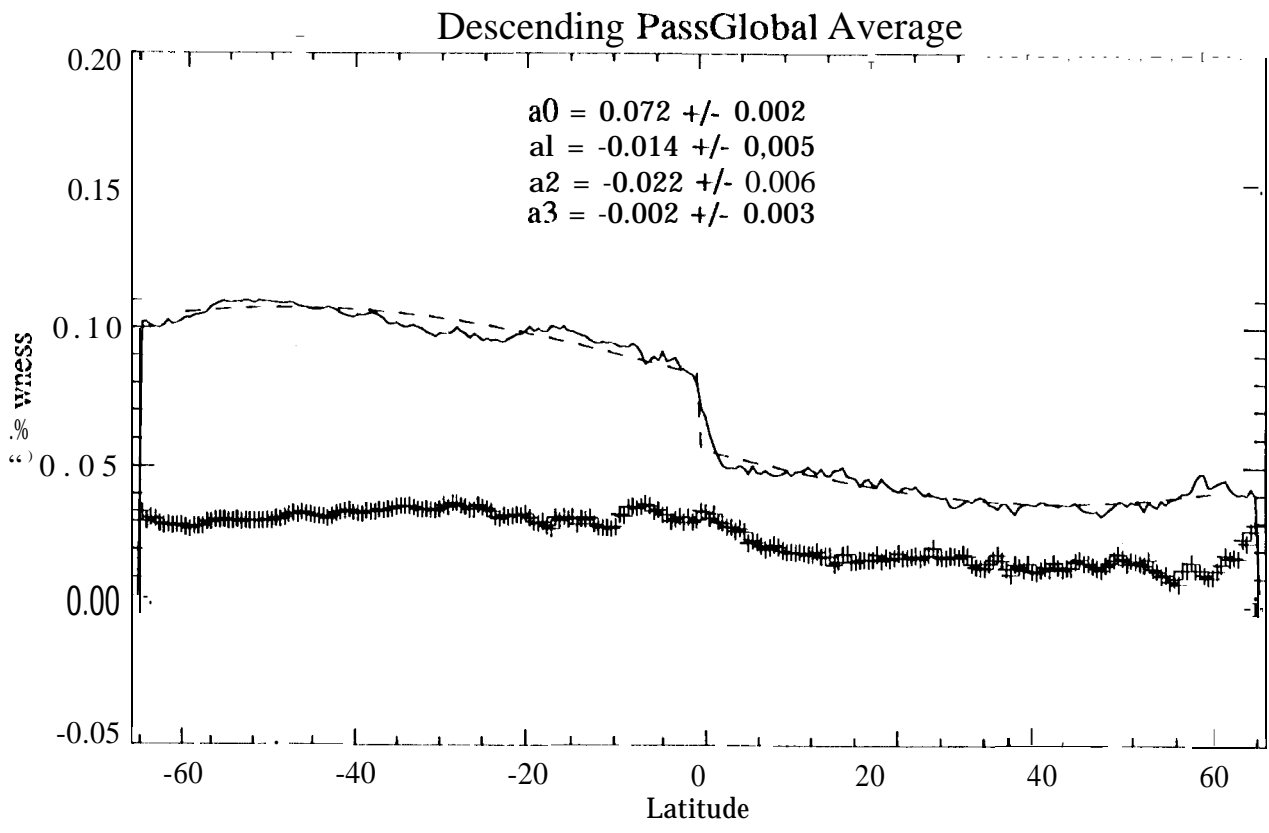
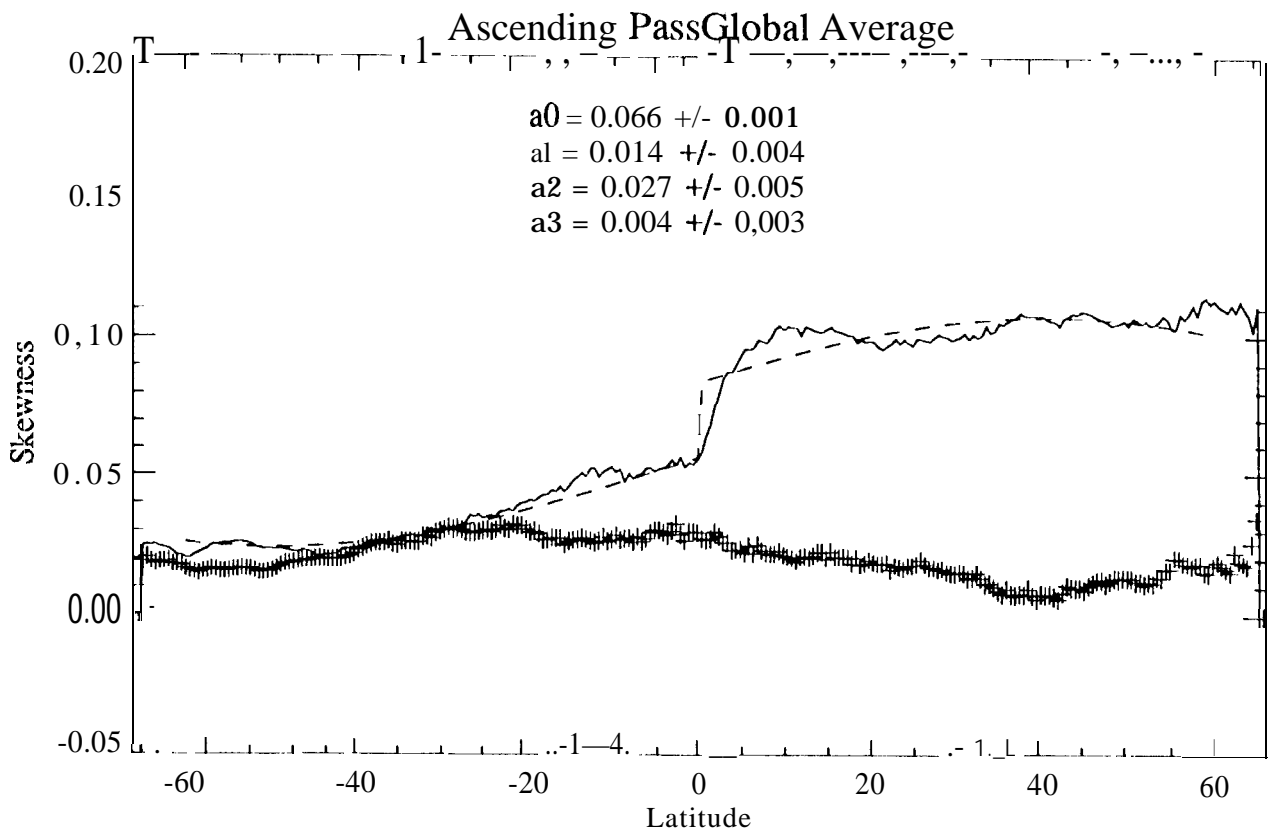


Figure 5

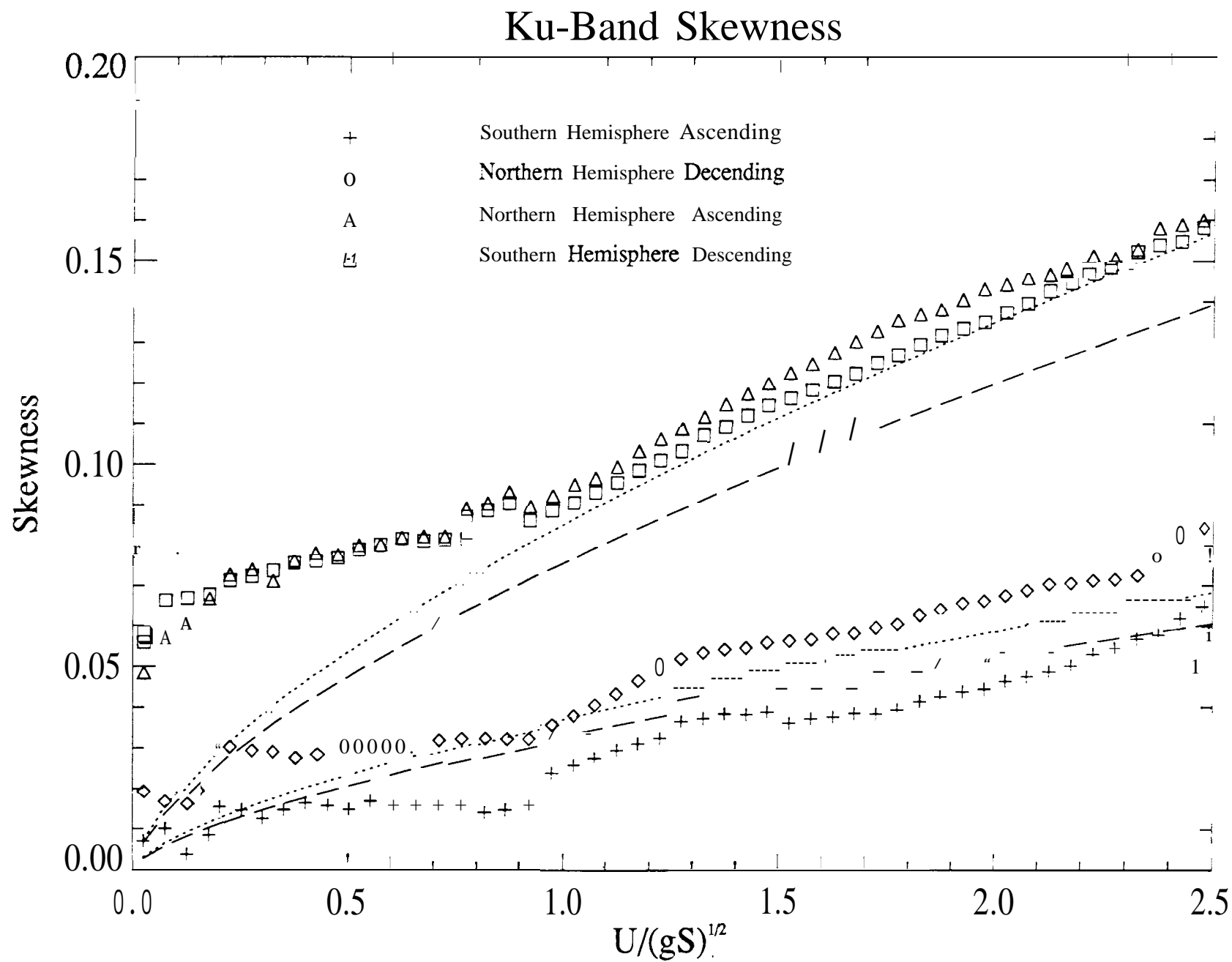


Figure 6

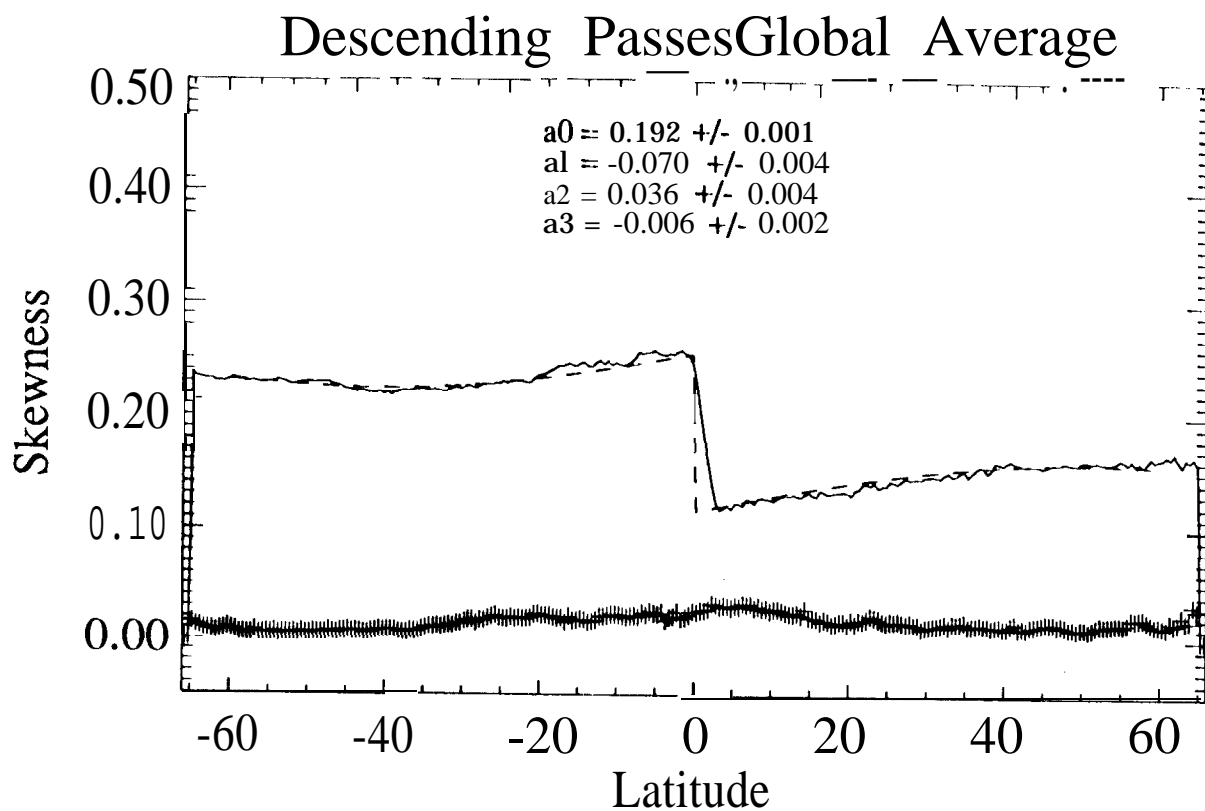
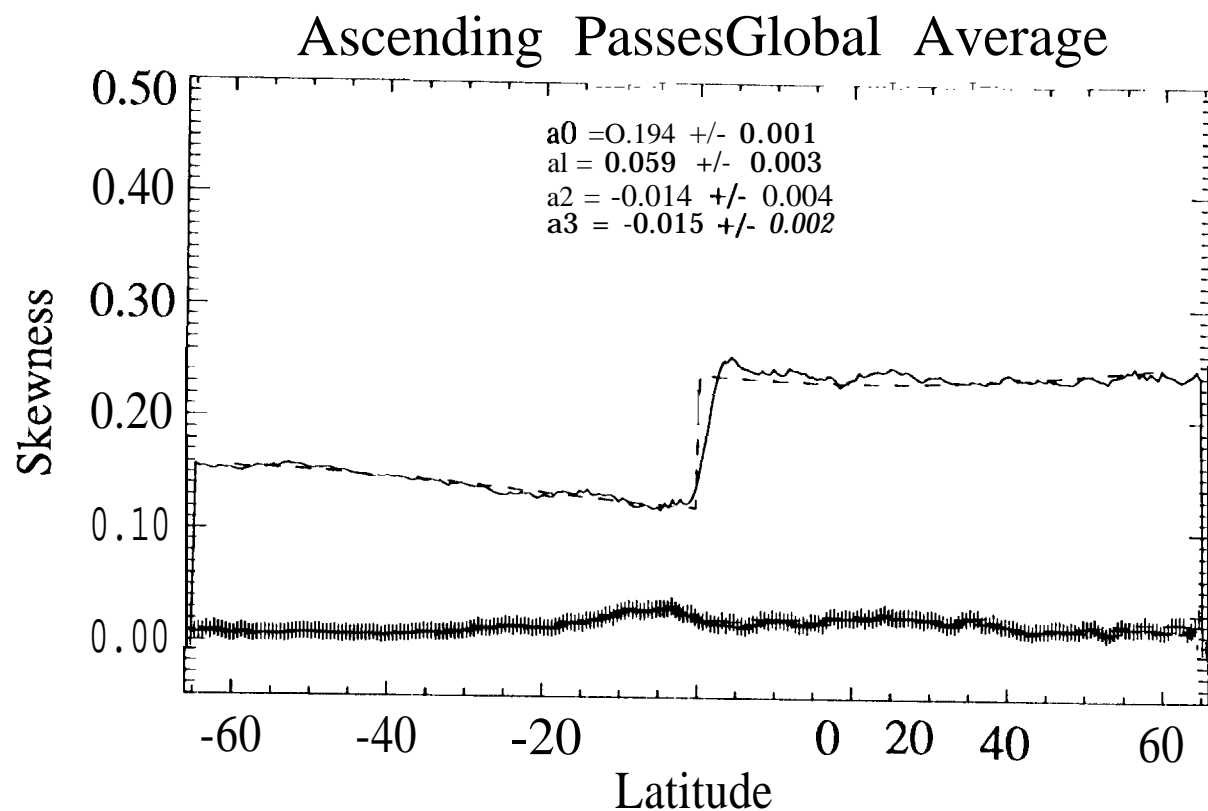


Figure 7

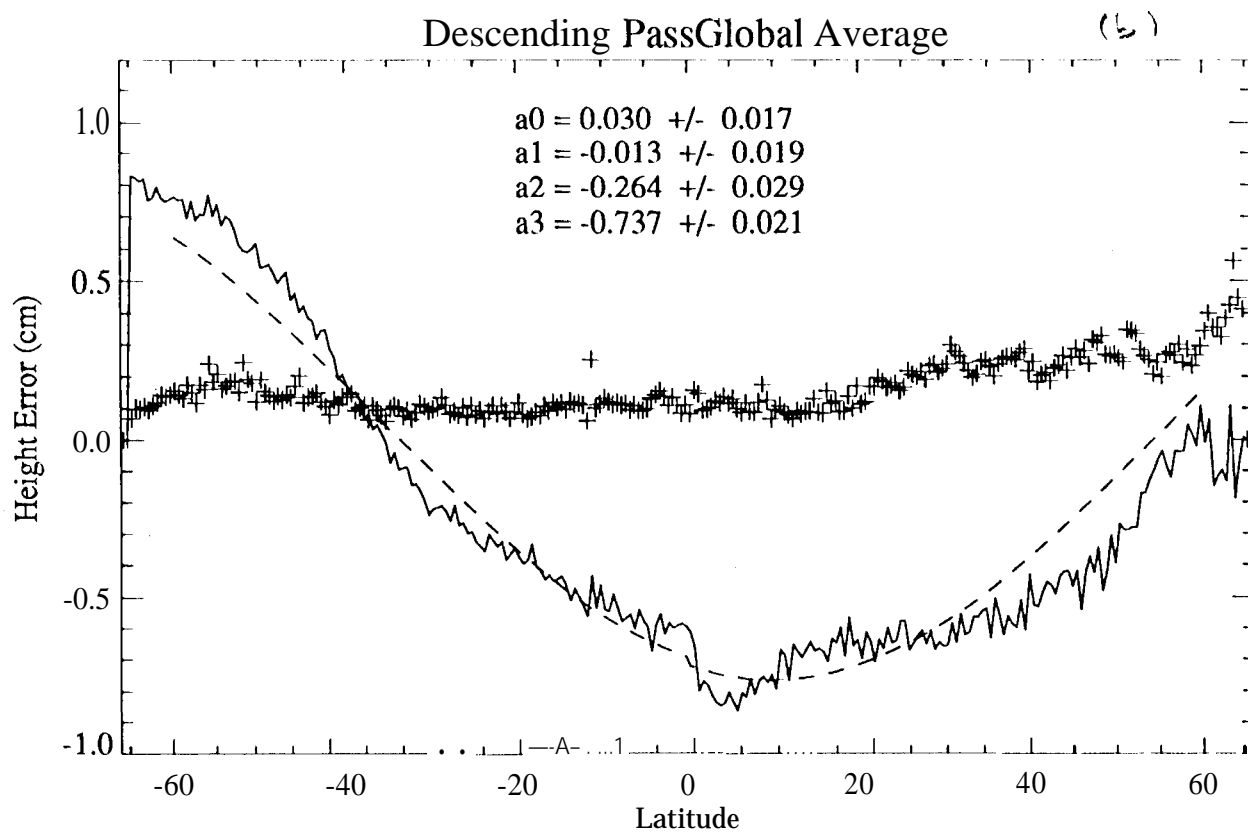
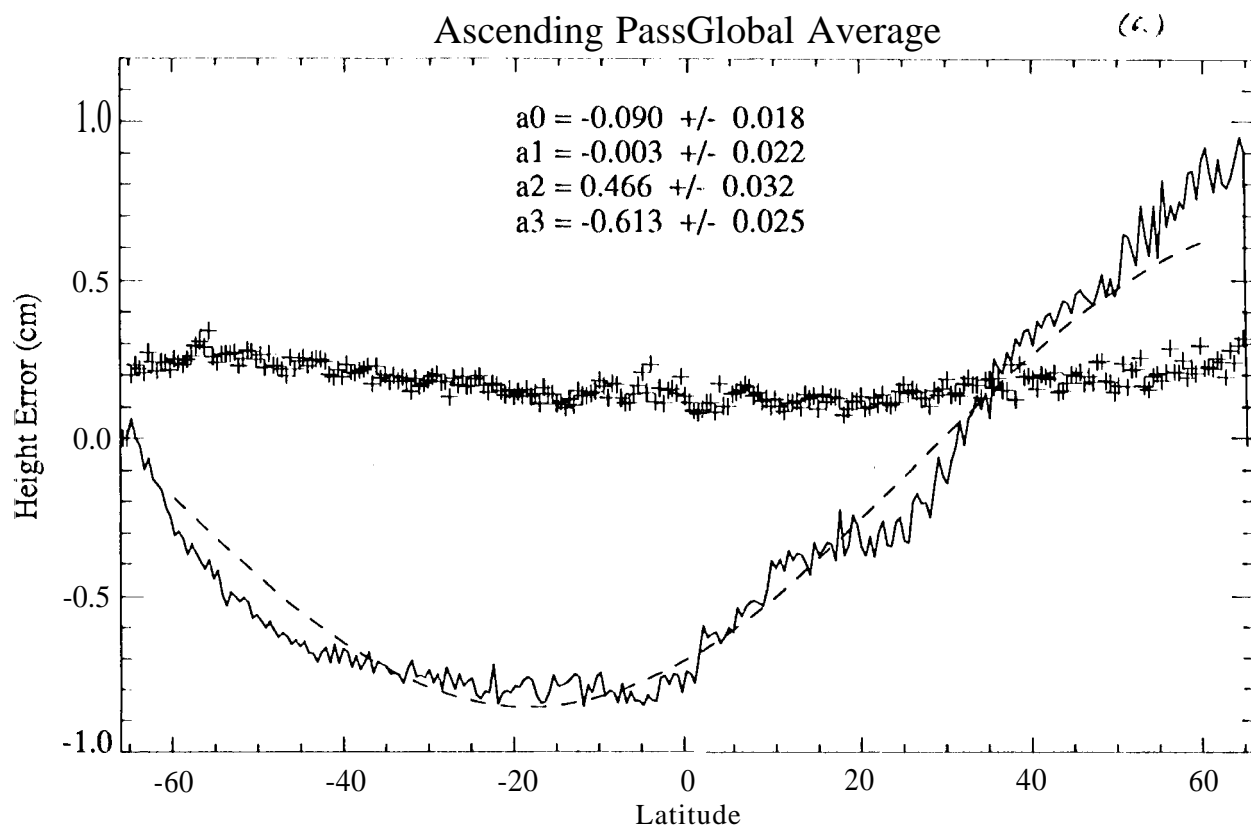


Figure 8

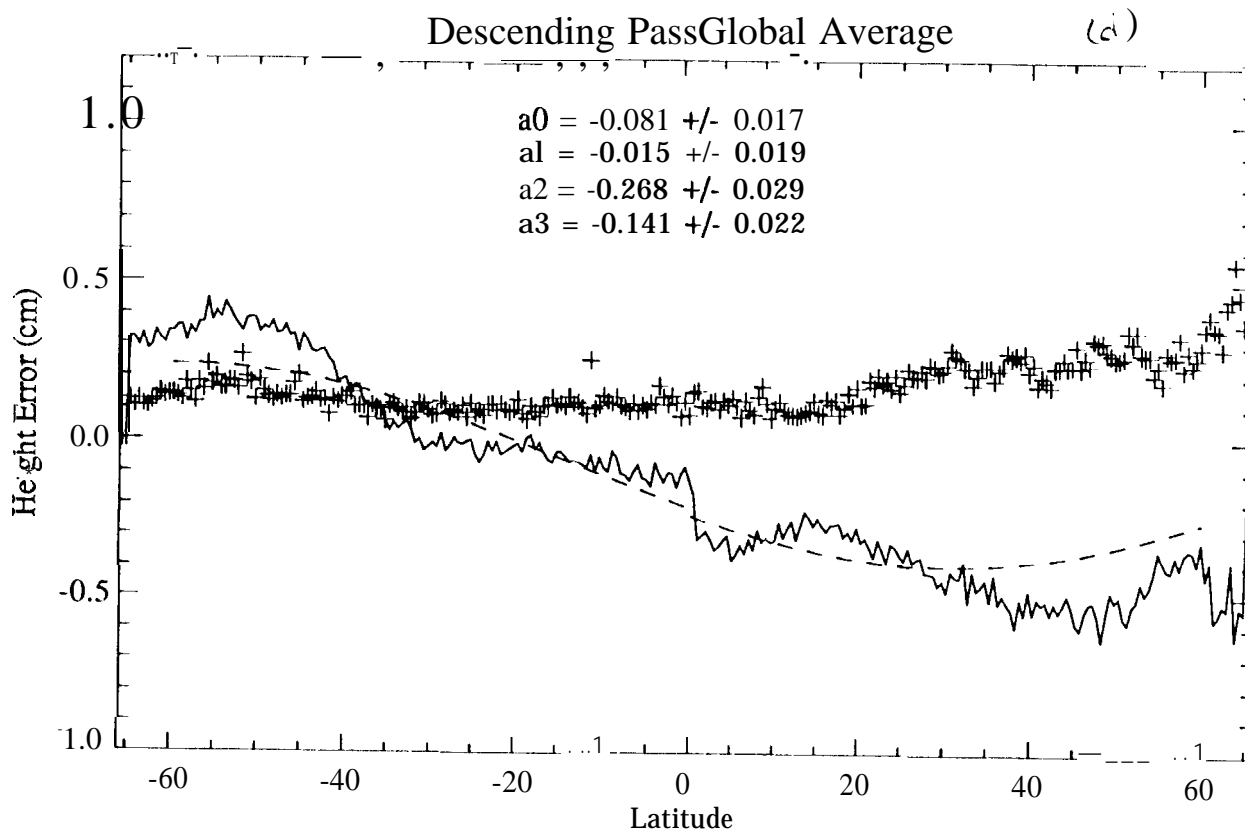
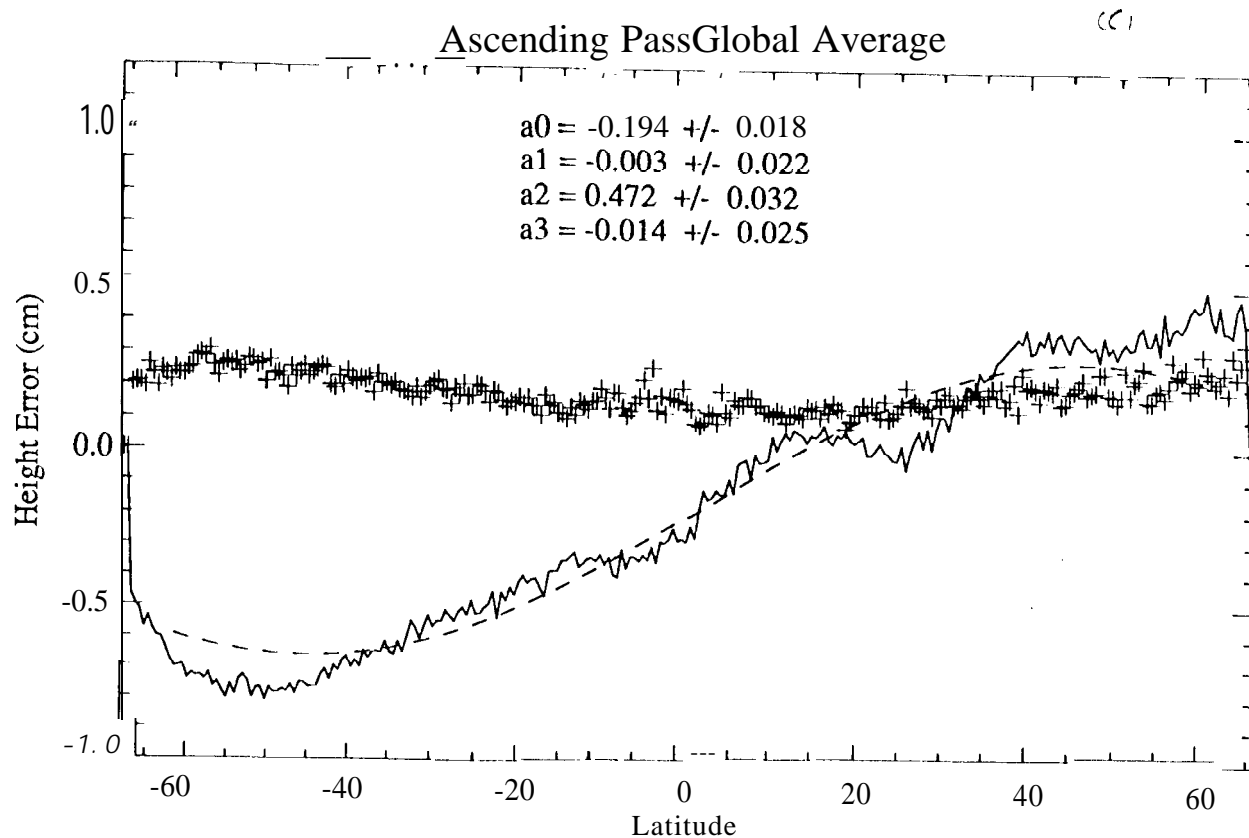


Figure 8

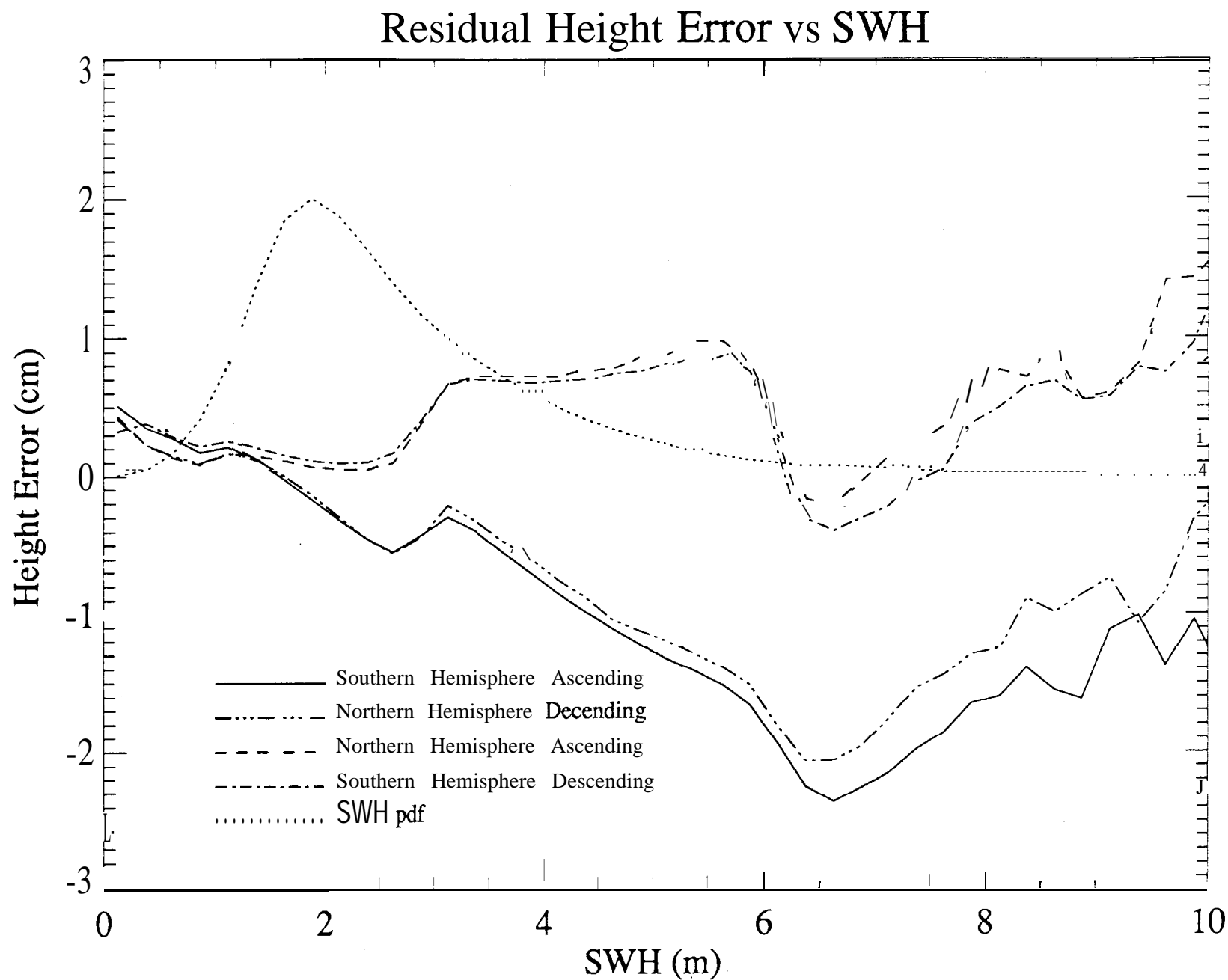


Figure 9

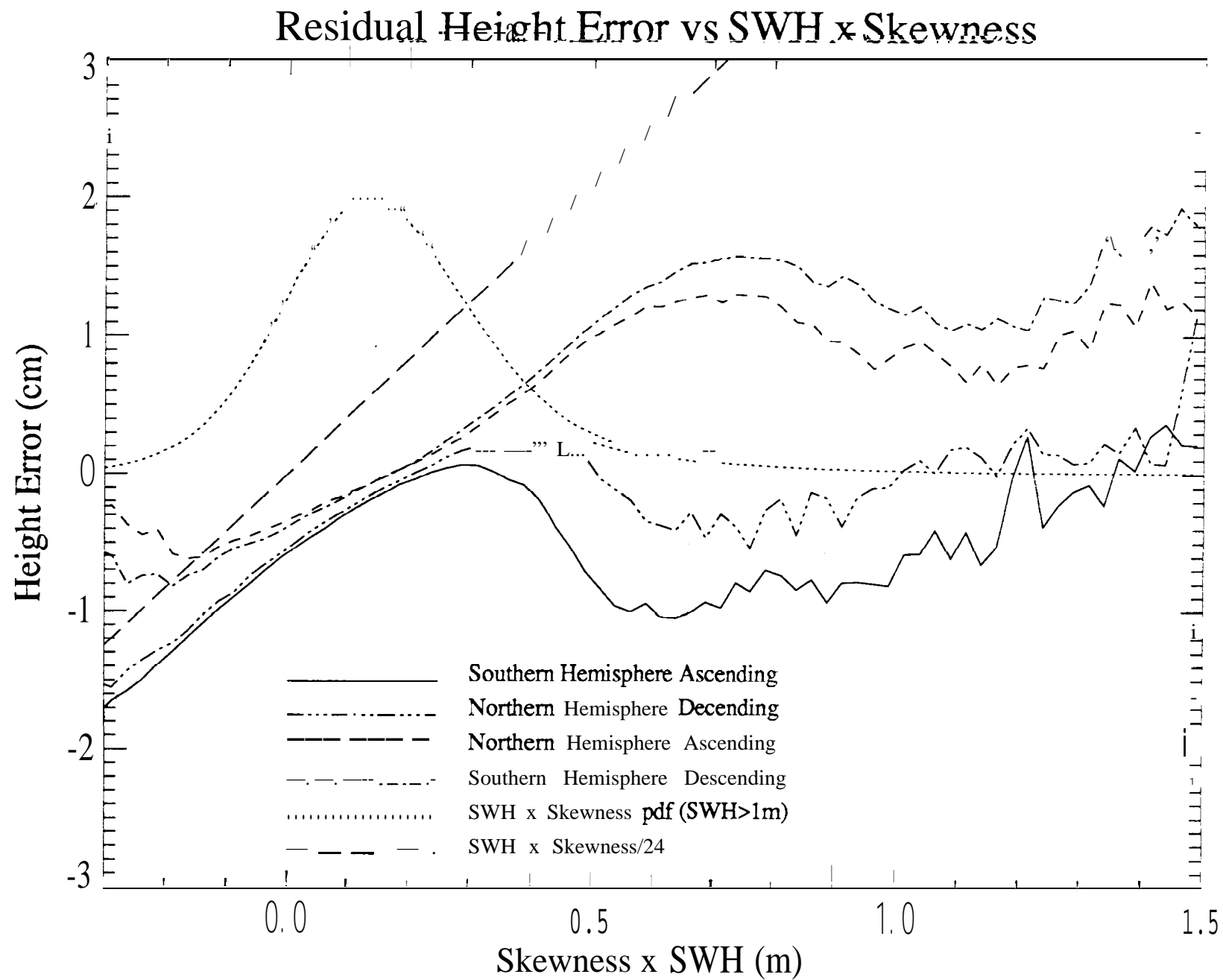


Figure 10

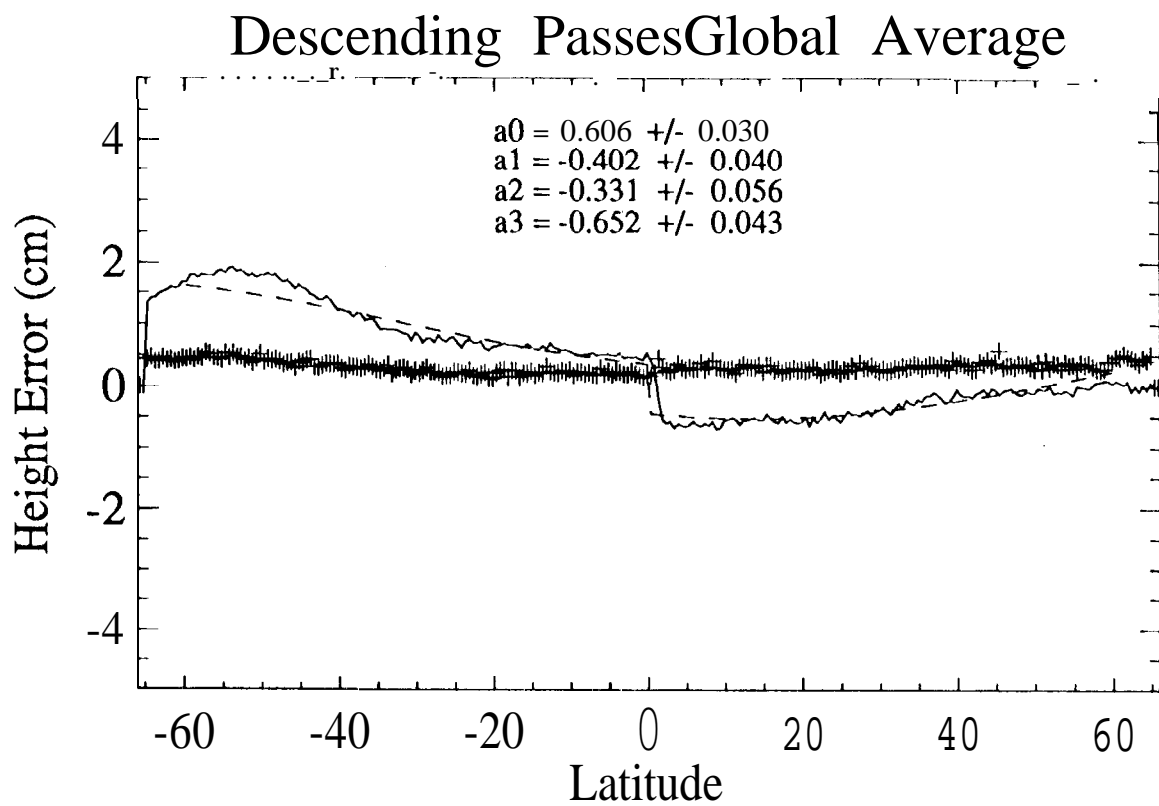
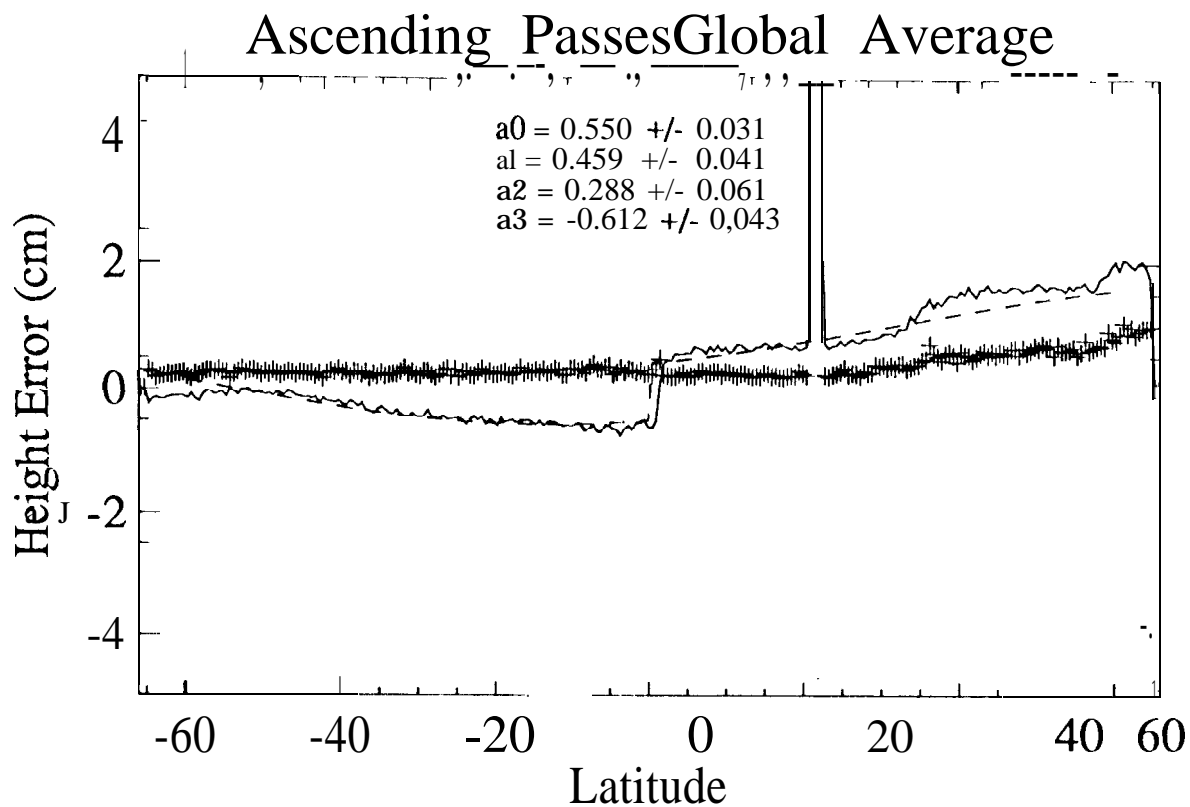


Figure 11

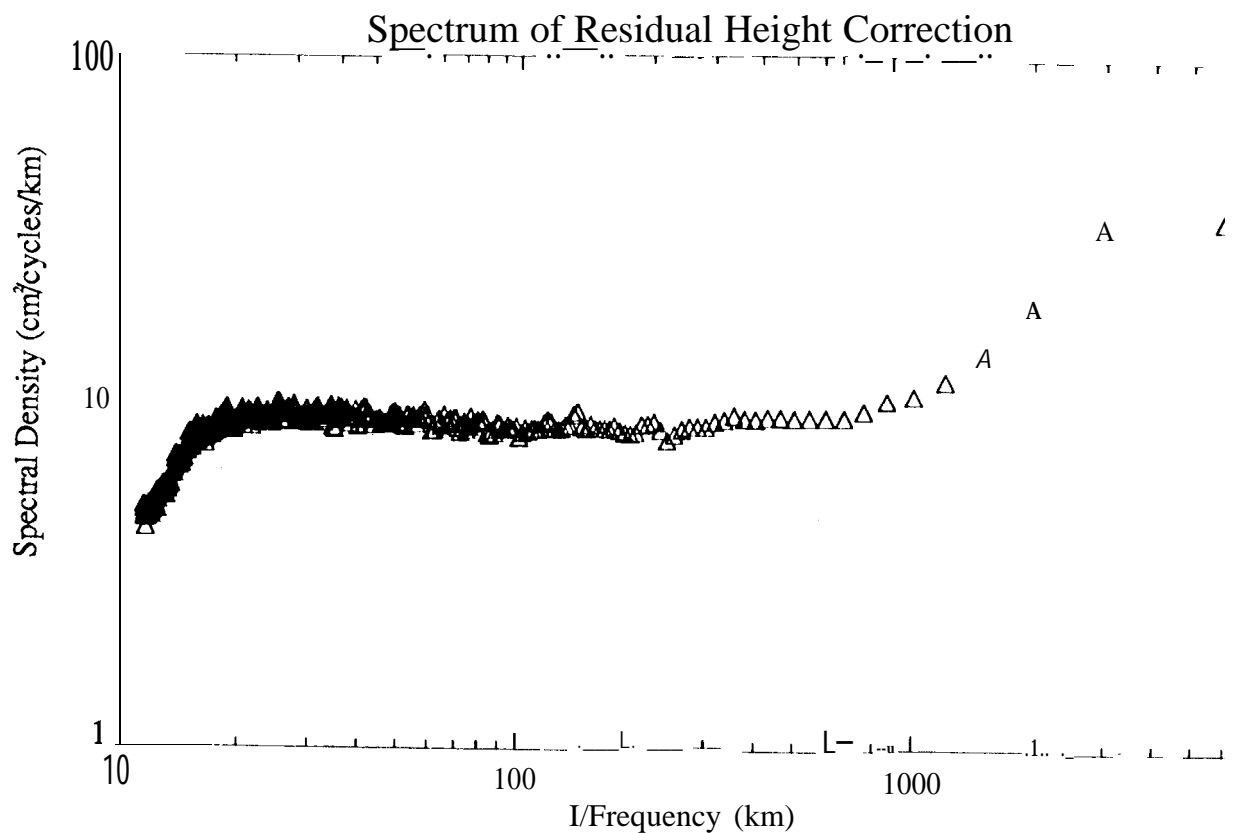
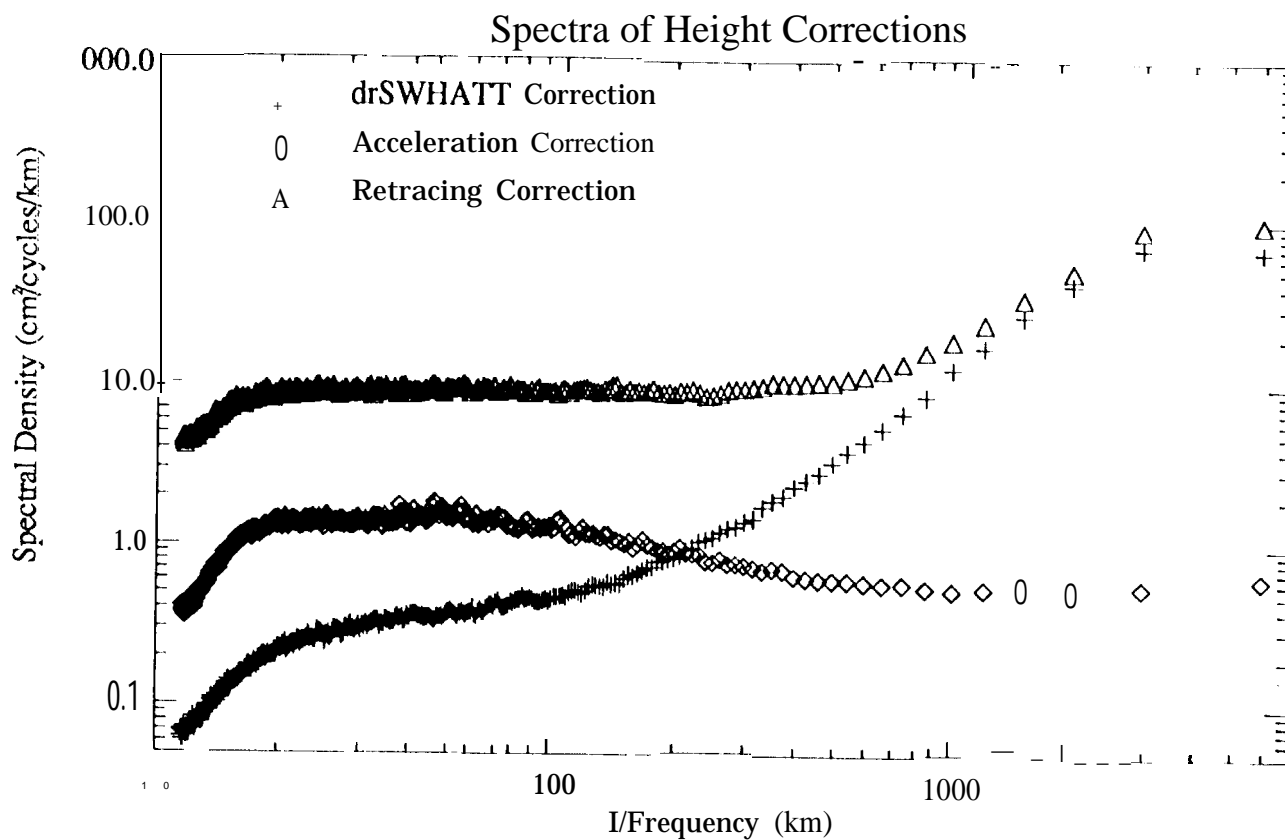


Figure 12.

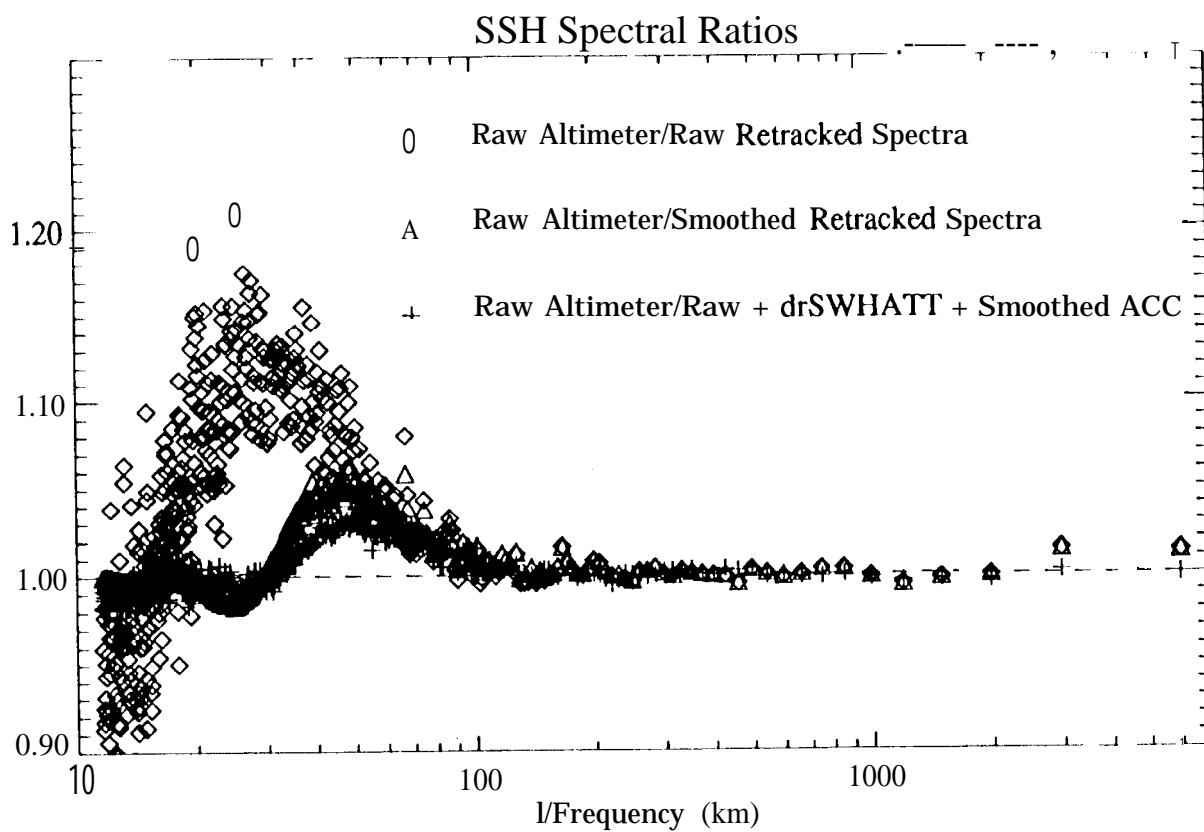
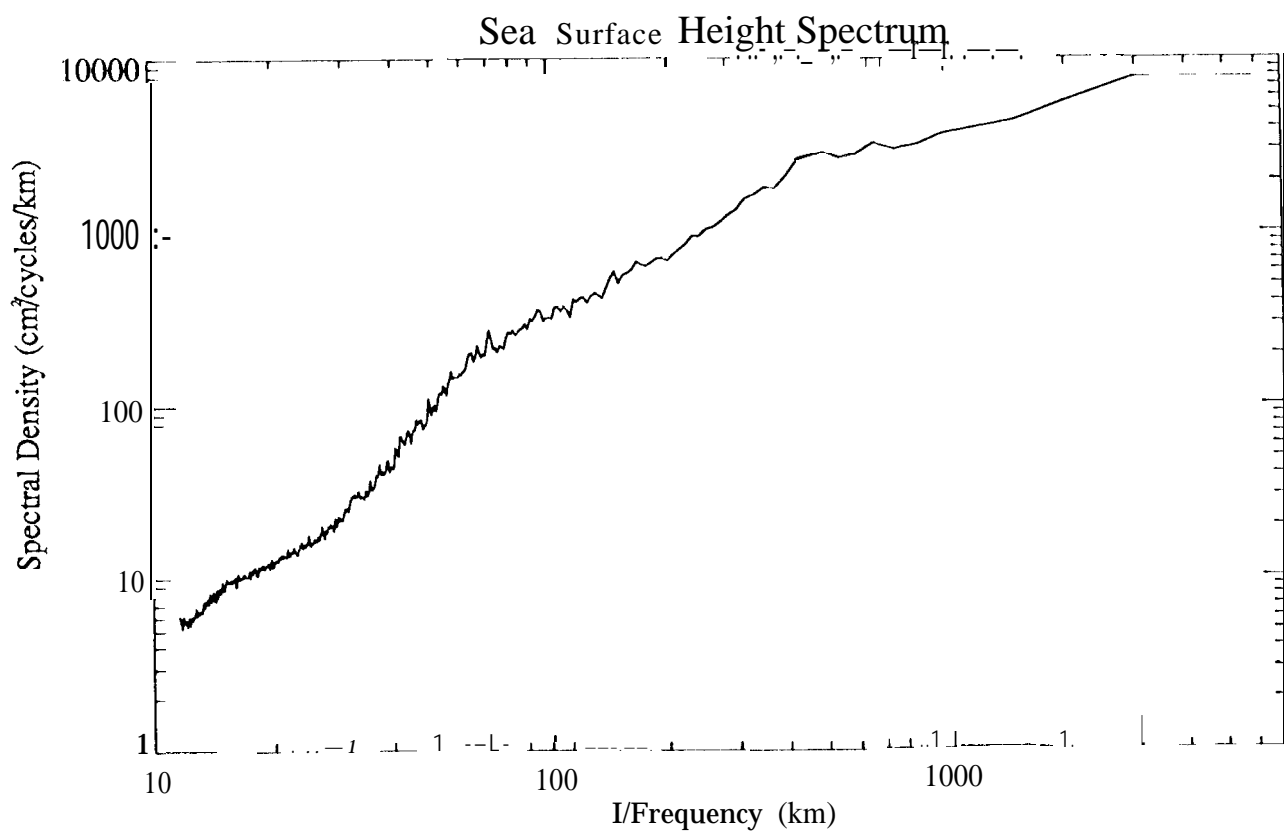


Figure 13

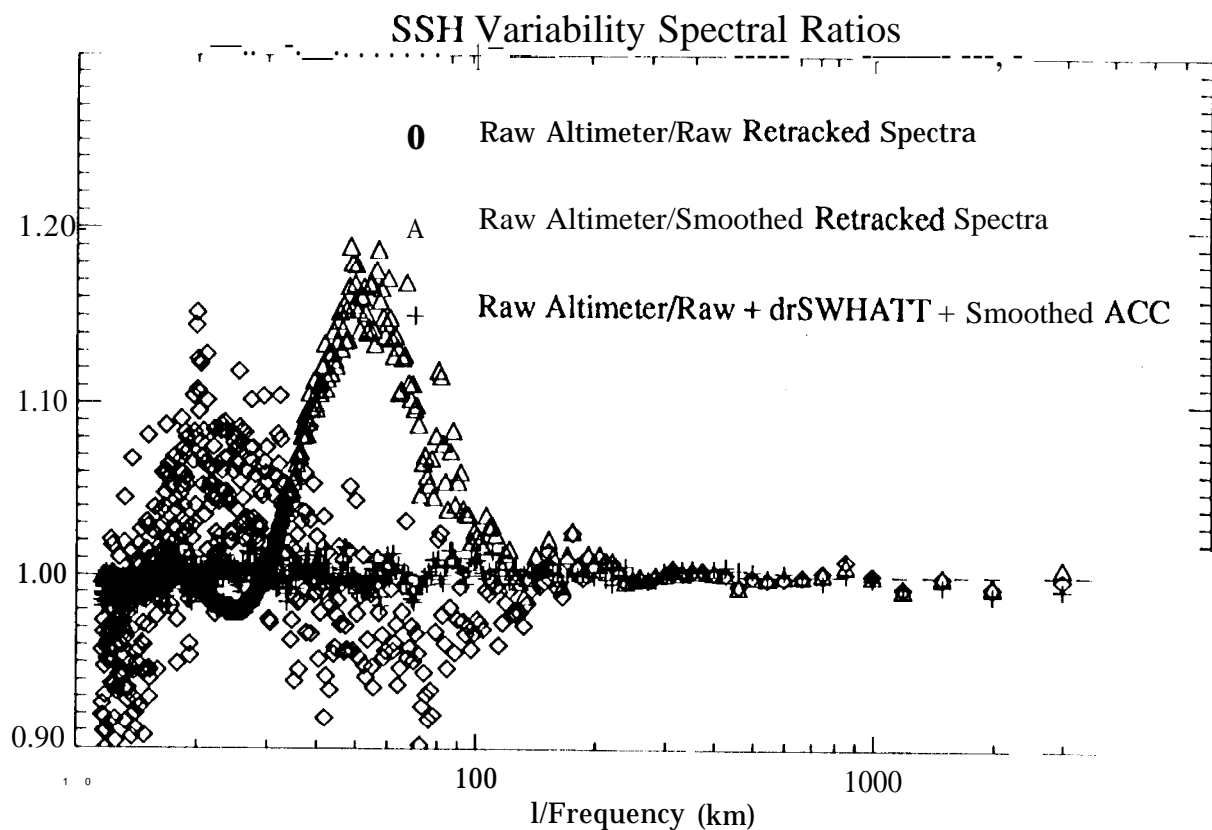
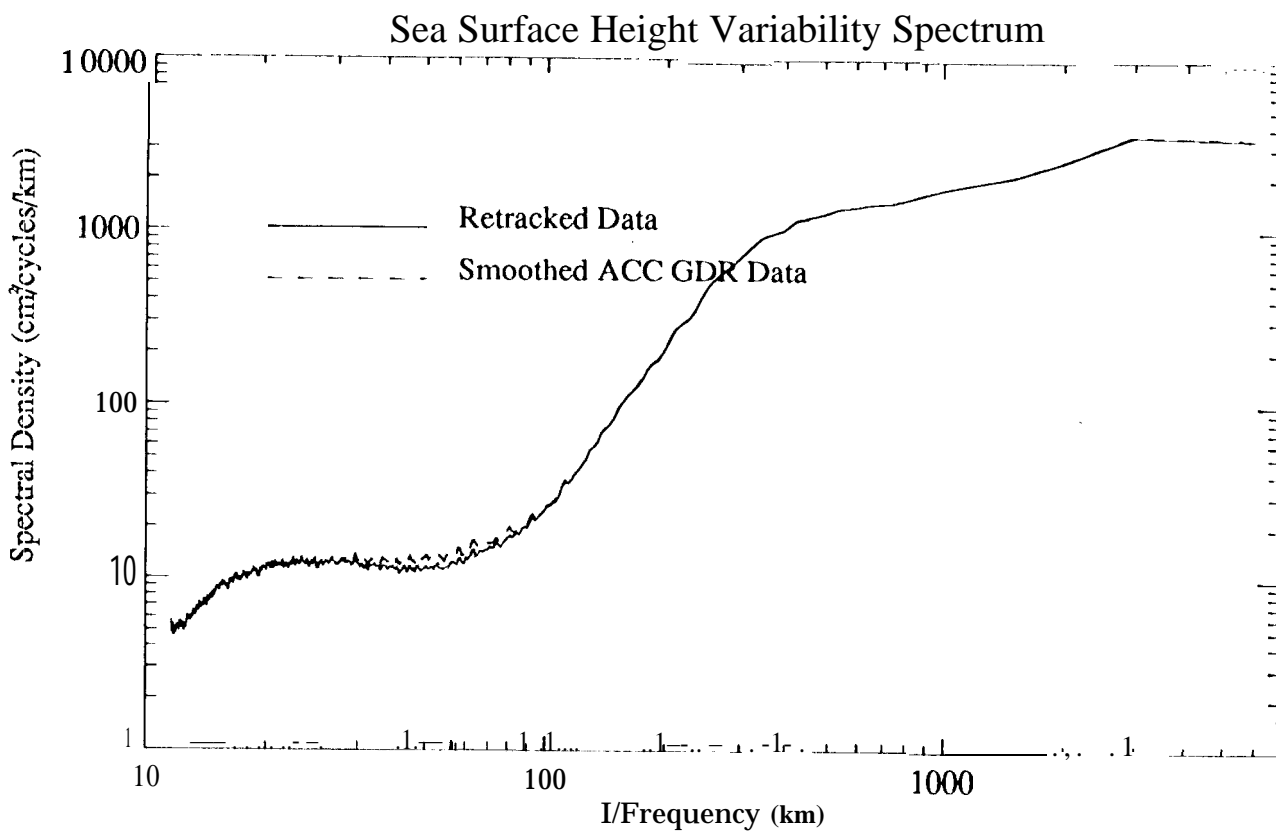
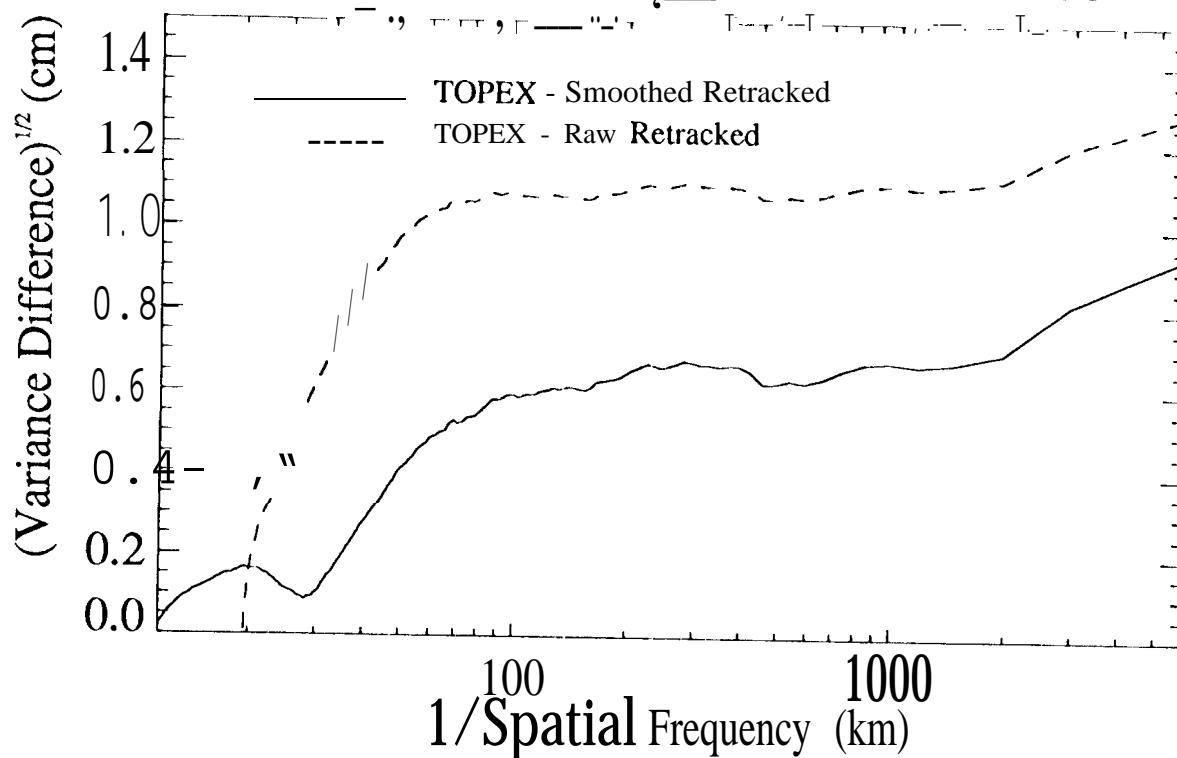


Figure 14

TOPEX Additional SSH Variance ^(a)



TOPEX Additional SSH Variability Variance ^(b)

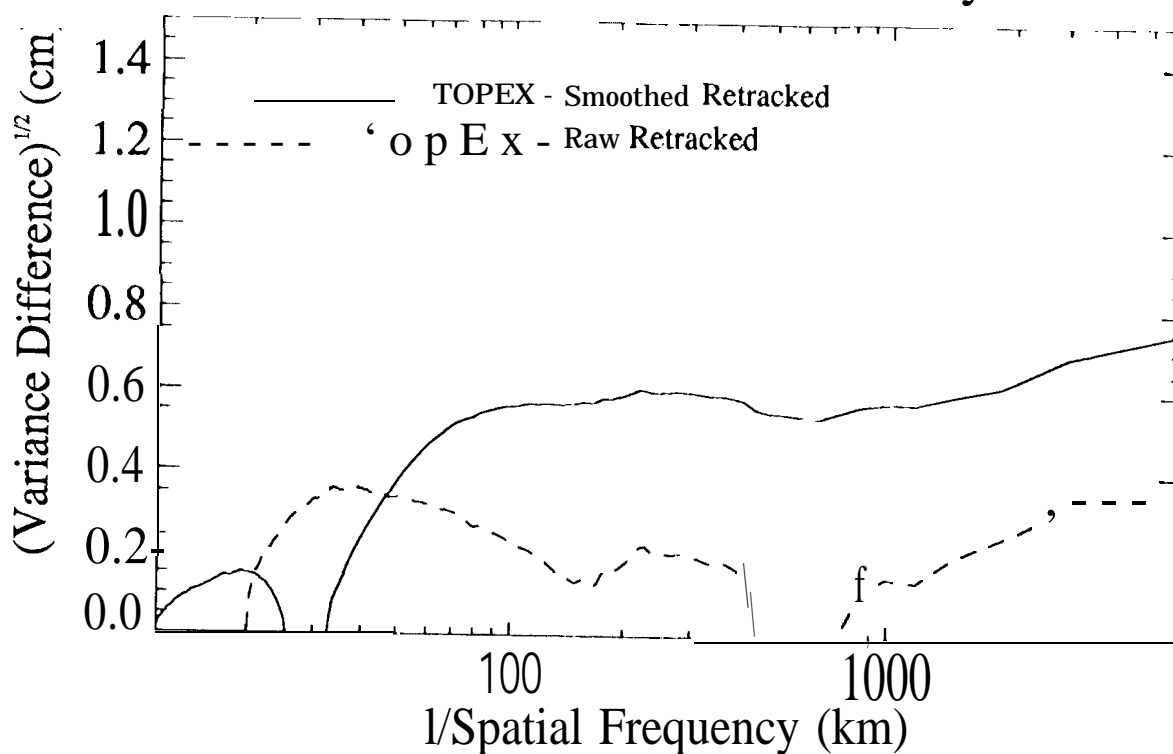


Figure 15